ELEMENTA
Science of the Anthropocene

Oziel, L, et al. 2019. Environmental factors influencing the seasonal dynamics of spring algal blooms in and beneath sea ice in western Baffin Bay. *Elem Sci Anth,* 7: 34. DOI: https://doi.org/10.1525/elementa.372

RESEARCH ARTICLE

Environmental factors influencing the seasonal dynamics of spring algal blooms in and beneath sea ice in western Baffin Bay

L. Oziel[*,†], P. Massicotte[*], A. Randelhoff[*], J. Ferland[*], A. Vladoiu[‡], L. Lacour[*], V. Galindo[§,¶], S. Lambert-Girard[*], D. Dumont[§], Y. Cuypers[‡], P. Bouruet-Aubertot[‡], C.-J. Mundy[¶], J. Ehn[¶], G. Bécu[*], C. Marec[*,‖], M.-H. Forget[*], N. Garcia[**], P. Coupel[*,**], P. Raimbault[**], M.-N. Houssais[‡] and M. Babin[*]

Arctic sea ice is experiencing a shorter growth season and an earlier ice melt onset. The significance of spring microalgal blooms taking place prior to sea ice breakup is the subject of ongoing scientific debate. During the Green Edge project, unique time-series data were collected during two field campaigns held in spring 2015 and 2016, which documented for the first time the concomitant temporal evolution of the sea ice algal and phytoplankton blooms in and beneath the landfast sea ice in western Baffin Bay. Sea ice algal and phytoplankton blooms were negatively correlated and respectively reached 26 (6) and 152 (182) mg of chlorophyll *a* per m^2 in 2015 (2016). Here, we describe and compare the seasonal evolutions of a wide variety of physical forcings, particularly key components of the atmosphere–snow–ice–ocean system, that influenced microalgal growth during both years. Ice algal growth was observed under low-light conditions before the snow melt period and was much higher in 2015 due to less snowfall. By increasing light availability and water column stratification, the snow melt onset marked the initiation of the phytoplankton bloom and, concomitantly, the termination of the ice algal bloom. This study therefore underlines the major role of snow on the seasonal dynamics of microalgae in western Baffin Bay. The under-ice water column was dominated by Arctic Waters. Just before the sea ice broke up, phytoplankton had consumed most of the nutrients in the surface layer. A subsurface chlorophyll maximum appeared and deepened, favored by spring tide-induced mixing, reaching the best compromise between light and nutrient availability. This deepening evidenced the importance of upper ocean tidal dynamics for shaping vertical development of the under-ice phytoplankton bloom, a major biological event along the western coast of Baffin Bay, which reached similar magnitude to the offshore ice-edge bloom.

Keywords: Under-ice bloom; Phytoplankton and sea ice algae; Arctic Ocean; Baffin Bay; Environmental conditions; Light and mixing

1. Introduction

During the last four decades, the Arctic Ocean's climate has undergone rapid changes clearly evidenced by the spectacular decline in sea ice extent and thickness, as well as the length of the ice season (Kwok, 2018; Stroeve and Notz, 2018; Serreze and Meier, 2019). Sea ice is an important driver of marine primary production and consequently the whole ecosystem (Post et al., 2013; Meier, 2016). First, the sea ice matrix provides a habitat for microalgae which are incorporated into brine channels during freezing in fall (Arrigo, 2017). Second, sea ice with its snow cover controls the amount of light that penetrates into the underlying water column (e.g., Mundy et al., 2007; Frey et al., 2011; Assmy et al., 2017), and thus the potential photosynthetic

---

[*] Takuvik Joint International Laboratory, Laval University (Canada) – CNRS (France), Département de biologie et Québec-Océan, Université Laval, Québec, CA

[†] Remote Sensing Unit, Bedford Institute of Oceanography, Fisheries and Oceans Canada, Dartmouth, Nova Scotia, CA

[‡] Sorbonne Université (UPMC, Paris6)/CNRS/UPMC/IRD/MNHN, Laboratoire d'Océanographie et du Climat (LOCEAN), Institut Pierre Simon Laplace (IPSL), FR

[§] Institut des sciences de la mer de Rimouski, Université du Québec à Rimouski, Allée des Ursulines, Rimouski, Québec, CA

[‖] Laboratoire d'Océanographie Physique et Spatiale, CNRS – IFREMER – IRD – UBO, Plouzané, FR

[¶] Centre for Earth Observation Science, University of Manitoba, Winnipeg, Manitoba, CA

[**] Aix-Marseille University, Mediterranean Institute of Oceanography (MIO), CNRS/INSU, IRD, Marseille, FR

Corresponding author: L. Oziel (laurent.oziel@takuvik.ulaval.ca)

activity of microalgae (Leu et al., 2015). Sea ice growth and melt affect the processes responsible for the supply of nutrients to the upper ocean by influencing stratification and mixing (Randelhoff et al., 2017). Recently, the importance of how the changing sea ice affects the under-ice dynamics of microalgae has been recognized in other regions; however, little is known about Baffin Bay (**Figure 1**).

Low-light conditions are recognized to sustain ice algal growth (Leu et al., 2015; Lacour et al., 2017; Hancke et al., 2018). Although contributions of ice algae to the annual primary production remain highly variable, depending on the season and the region (<1 to 60%; e.g., Loose et al., 2011; Dupont, 2012; Fernández-Méndez et al., 2015), they are a critical food source for the marine food web especially during the winter (Søreide et al., 2010). The seasonal increase in solar radiation and the subsequent snow and sea ice melt lead to the termination of the ice algal bloom and to an increase in transmitted light and stratification underneath the sea ice (Mundy et al., 2014). This combined effect favors high phytoplankton growth in ice-covered waters as previously documented in the Arctic Ocean (e.g., Fortier et al., 2002; Mundy et al., 2009; Assmy et al., 2017). Under-ice phytoplankton blooms can reach magnitudes similar to or even greater than those observed in the open ocean with carbon fixation rates exceeding 30 g C m^{-2} d^{-1} in one documented instance (Arrigo et al., 2014), and are thought to account for more than half of the net algal community production in the Canadian Archipelago (Matrai and Apollonio, 2013).

The Western coast of Baffin Bay in the Canadian Arctic is an Arctic Ocean outflow shelf (**Figure 1**, Tang et al., 2004; Carmack and Wassmann, 2006). A stable landfast sea ice cover forms along the coast and creates a boundary against the offshore mobile ice pack. The static landfast sea ice has a relatively homogeneous thickness compared to pack ice, favoring the spreading of meltwater on the surface after the onset of snow melt in late spring and the formation of high melt pond coverage (Landy et al., 2015). The presence of melt ponds on the ice surface increases the transmission of light through the sea ice, which can trigger under-ice phytoplankton blooms (Mundy et al., 2009; Ehn et al., 2011; Frey et al., 2011; Arrigo et al., 2012). As part of the Green Edge project, this paper presents a comprehensive and unique time series of physical, chemical and biological parameters collected during two consecutive years, 2015 and 2016, in western Baffin Bay. The study objectives are to describe the physical processes at play, from the atmosphere, the snow, and the sea ice to the upper ocean, and to identify their roles in modulating the ice algal and phytoplankton spring bloom. While this paper focuses on the temporal variability beneath the landfast sea ice, an additional paper will investigate the physical processes controlling the bloom in time and space in the Baffin Bay marginal ice zone during the Canadian Coast Guard Ship (CCGS) *Amundsen* cruise in 2016 (Randelhoff et al., 2019).

2. Materials and methods

The study site was located near the community of Qikiqtarjuaq, south of Qikiqtarjuaq Island, along the eastern coast of Baffin Island (67.48 N, 63.79 W, 350-m water depth), and tightly connected with the Baffin Bay through

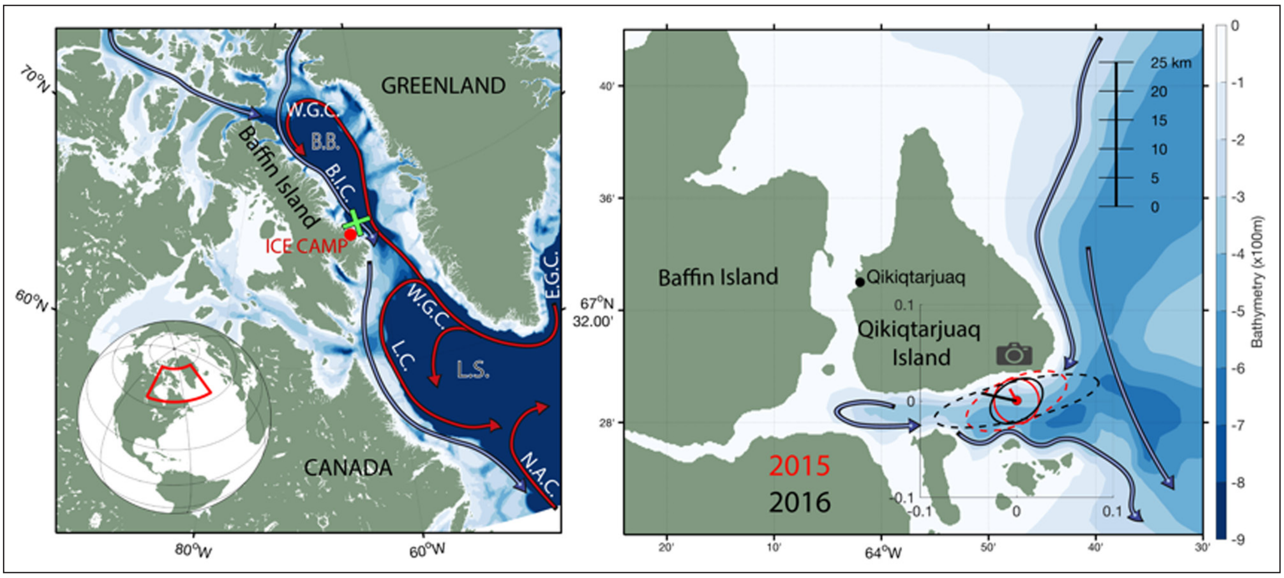

Figure 1: Maps of Baffin Bay, surrounding seas and study site. Baffin Bay and its general surface circulation in the Eastern Canadian Arctic Ocean under Atlantic (red) or Pacific (blue) water influence. The study site (ICE CAMP), south of Qikiqtarjuaq Island, is indicated by a red dot. The green cross indicates station 403, the nearest station sampled by the CCGS *Amundsen* off the continental slope in 2016. Dashed and solid lines represent the variance ellipses of the predicted tidal currents and the daily mean velocities (m s^{-1}), respectively. The arrows show the direction and magnitude of the mean velocity fields at 10 m over the full period (2015 in black, 2016 in red). The camera pictogram indicates the position where the time-lapse pictures were taken. Abbreviations: Baffin Island Current (B.I.C.), Baffin Bay (B.B.), East Greenland Current (E.G.C.), Labrador Current (L.C.), Labrador Sea (L.S.), North Atlantic Current (N.A.C.), West Greenland Current (W.G.C.). DOI: https://doi.org/10.1525/elementa.372.f1

a 600-m deep trough (Gilbert, 1982) (**Figure 1**). The sampling was conducted during two consecutive years: from 28 March to 14 July 2015, and from 27 April to 22 July 2016. Sampling ended for the 2015 expedition on 14 July because the melting of sea ice close to the shore created dangerous conditions for snowmobile driving. However, in 2016, the use of an airboat on the fragile sea ice after 11 July allowed the extension our time series until 22 July 2016.

2.1. Snow and sea ice data

Every 2–3 days a sample site was chosen at an undisturbed location randomly selected within a 1.2-km radius throughout the project. At the sample site, 5–8 snow depth measurements were made with a metal ruler. A minimum of four ice cores were collected using an ice corer (2015: Kovacs Mark V 14-cm diameter corer for nutrients and algal biomass, Kovacs Mark IV 9-cm diameter corer for temperature and salinity; 2016: Kovacs Mark IV 9-cm diameter corer). The sea ice thickness and freeboard, i.e., the height of the sea ice surface from the sea surface, were measured through the ice core holes using a thickness gauge (Kovacs Enterprise). Two full ice cores were sampled as described in Miller et al. (2015) to measure vertical profiles of temperature and bulk salinity. Ice temperature was measured at 10-cm intervals using a high-precision thermometer (Testo 720; ±0.1°C). For ice salinity, the ice was cut with a handsaw into 10-cm sections, which were stored in plastic containers (Whirl-Pak bags) and later melted at room temperature. Bulk salinity of the melted ice sections was determined using a conductivity probe (2015: WTW 330i handheld conductivity meter; 2016: Thermo Scientific Orion portable salinometer model WP-84TPS) that was calibrated every sampling day with seawater standard (35) and MilliQ water (0). Brine volume fraction (%), a controlling factor for ice permeability, and brine salinity were calculated for each 10-cm section using the ice temperature and bulk salinity following Cox and Weeks (1983) and Leppäranta and Manninen (1988); see Gourdal et al. (2019) for a more detailed description of the method. For the biological and chemical analyses, at least two bottom 10-cm sections (0–3 cm and 3–10 cm layers) of ice cores were pooled in a 20-L dark isothermal container, with 10 volumes (ice/water ratio = 1/10) of filtered seawater (0.22 µm polyvinylidene fluoride filter, PVDF, Thermo Fisher Scientific) added to minimize osmotic stress on microalgae cells, and melted overnight (Bates and Cota, 1986; Garrison and Buck, 1986). Analyses (described in Section 2.4) were performed as soon as the ice had melted, or within 24 h, at room temperature (~15°C). The nutrients present in the filtered surface seawater were measured separately and corrected for final estimation of nutrient concentrations in the sea ice sections. In 2016, the filtered seawater was replaced by artificial seawater (MiliQ water with 35 g of Suprapur© NaCl) which did not contain nutrients.

Continuous measurements of wind speed and air temperature were recorded with a meteorological station positioned near (<100 m) the center of the 1.2-km radius (Automated Meteo Mat equipped with temperature (HC2S3) and wind (05305-L) sensors, Campbell Scientific). The day of the snow melt onset was identified as the date after which the snow thickness stopped increasing and when the air temperature approached 0°C during the day. A positive air temperature was associated with a strong decrease in the near-infrared (1000 nm) albedo (measured every sampling day with a custom-built radiometer, Solalb, LGGE), making it a good indicator for snow melt onset in our case (see Verin et al., 2019, for more details). Sea ice concentration was inferred from the satellite AMSR2 radiometer dataset on a 3.125-km grid (Spreen et al., 2008). The closest pixel of sea ice concentration was less than 500 m from the study site. The sea ice breakup was determined as the date when the sea ice concentration was below 80% and when major cracks appeared around the study site, i.e., when the sea ice at the study site detached from the landfast ice (Figures S1, S2). Melt ponding onset and ice breakup were determined visually in the field and cross-checked using: 1) a time-lapse camera installed on Qikiqtarjuaq Island at 300 m above sea level and aimed south (**Figure 1**), 2) pictures taken of the study site from an unmanned aerial vehicle (UAV) almost every sampling day, and 3) satellite data ('true color' images from Landsat-8 and Sentinel-2, Figures S1 and S2).

2.2. Optical measurements

In-water multispectral radiometric data were acquired every 2–3 days using an underwater spectroradiometer (IcePRO, Biospherical Instrument Inc.). The IcePRO is a modified version of the C-OPS made by the same manufacturer (Compact Optical Profiling System; Hooker et al., 2013) to measure downwelling irradiance ($E_d(z,\lambda)$) and upwelling radiance ($L_u(z,\lambda)$) under the ice to a depth z of up to 100 m, together with above surface downwelling irradiance $E_d(0^+,\lambda)$. Photosynthetically available radiation (PAR) at each depth ($PAR(z)$, mol photons m^{-2} s^{-1}) was calculated as follows:

$$PAR(z) = \int_{400}^{700} E_d(\lambda, z)\, d\lambda$$

Daily photosynthetically available radiation ($PAR_{24h}(z)$, mol photons m^{-2} d^{-1}) in the water column was calculated by multiplying surface $PAR_{24h}(0^+)$ by the instantaneous transmittance, $t(z)$, profile calculated from the C-OPS as follows:

$$PAR_{24h}(z) = PAR_{24h}(0+) \times t(z)$$

where $t(z) = PAR(z)/PAR(0^+)$. In 2015, downwelling shortwave irradiance K (W m^{-2}) was acquired using a pyranometer (CNR4, Kipp and Zonen) between 300 nm and 2800 nm. We then calculated PAR using the following formula

$$\text{PAR} = \frac{fract \times K \times cf \times 10^6}{N_A}$$

where cf = 2.77 10^{18} photon s^{-1} W^{-1} (Morel and Smith, 1974), N_A is Avogadro's number, and the factor of 10^6 is used to convert from mol photons to µmol photons. The

PAR fraction, *fract*, was modulated by a function of the solar zenith angle following Kirk (2011) and references therein. In 2016, downwelling PAR was directly measured using a LI-190SA instrument (Li-COR). On regular occasions, instrument failure resulted in missing $PAR_{24h}(0^+)$ measurements (24 d in 2015 and 5 d in 2016). For these days, $PAR_{24h}(0^+)$ was computed every 3 h using the Santa Barbara DISORT Atmospheric Radiative Transfer model (SBDART, Ricchiazzi et al., 1998) as described in Bélanger et al. (2013) and Laliberté et al. (2016).

Under a spatially heterogeneous surface of sea ice and snow, measuring a representative attenuation coefficient over a given large area is challenging because the profiles are characterized by subsurface light maxima occurring between depths of 5 and 10 m. To reduce the effect of sea ice surface heterogeneity on irradiance measurements (e.g., Ehn et al., 2011, Frey et al., 2011; Katlein et al., 2015), the vertical attenuation coefficients of PAR, $K_d(PAR)$, were calculated by fitting a single exponential function on PAR profiles between 10 and 50 m. Then, estimated $K_d(PAR)$ was used to estimate PAR at 1.3 m (*PAR(1.3m)*; for more details, see Massicotte et al., 2018). Note that 1.3 m corresponds to the average ice thickness measured during the field campaign and thus to the first measure under the ice.

In the present study, the euphotic zone is defined as the layer between the surface and the depth where $PAR_{24h}(z)$ = 0.415 mol photons m^{-2} d^{-1}, denoted $Z_{0.415}$. We prefer to define the euphotic zone in absolute rather than relative terms (cf. the usual 1% depth) because of large seasonal variations in incident irradiance at high latitudes, as well as sustained low levels even during the summer due to sea ice. The threshold adopted here was found to match the 1% depth in the subtropical North Pacific by Letelier et al. (2004), and was later used by Boss and Behrenfeld (2010). Lacour et al. (2015) used a lower threshold of 0.1 mol photons m^{-2} d^{-1} for the North Atlantic. Letelier et al. (2004) measured scalar irradiance using a spherical sensor, while the C-OPS used in this study measures planar irradiance. Field measurements at the study site (Matthes et al., 2019) indicate that the conversion from planar to scalar irradiance relies on a multiplying factor of ~1.4 within the upper 20 m of the water column. With the companion paper (Randelhoff et al., 2019), we estimated that by using planar irradiance, the isolume depths are underestimated by approximately 1–7 m. The isolume depths in this study are thus conservative and indicate the depth range at which microalgal growth is greatly favored, but they are not based on a physiological response.

2.3. Hydrographical data and methods

Conductivity, temperature and depth (CTD) profiles were collected using a Sea-Bird Electronics 19plus V2 CTD system (factory calibrated prior to the expedition) deployed from a 1-m^2 hole in the ice under a tent (Polarhaven, Weatherhaven) from the surface water down to 350 m. The data were post-processed according to the standard procedures recommended by the manufacturer and averaged into 1-m vertical bins. Ocean current profiles in the water column were measured using a downward looking 300 kHz Sentinel Workhorse Acoustic Doppler Current Profiler (ADCP) by RDI Teledyne mounted just beneath the sea ice bottom through a 25-cm auger hole. The first valid bin was located at a depth of about 4 m; subsequent bins were spaced with a 2-m vertical resolution and data were collected every 30 min. Flagged data due to large tilt angles as well as data associated with estimated errors (percentage of the signal variance) above 50% were rejected, which led us to consider only the data from depths between 7 and 40 m. Data were also corrected for the magnetic declination. Mean current velocities ($\sqrt{\bar{u}^2+\bar{v}^2}$) were obtained by daily averaging.

To identify the origins of the water masses in 2015 and 2016, we derived the "Arctic N-P relationship" (ANP; Jones et al., 1998; Newton et al., 2013), which basically distinguishes between waters with Atlantic (ANP = 0) and Pacific (ANP = 1) signatures based on the $[NO_3]$ vs $[PO_4]$ relationship (Figure S3). More details on this method are described in Newton et al. (2013) and Randelhoff et al. (2019).

We derived a winter mixed layer depth (MLD; Rudels et al., 1996) "baseline" for the study (Figure S4) based on late April measurements. MLD is the bottom of the density mixed layer, which is defined as the shallowest depth at which the density exceeds a critical density difference ($\Delta\sigma$ = 0.1 kg m^{-3}; see Peralta-Ferriz and Woodgate, 2015), relative to the surface density. Such a conventional MLD algorithm is less useful later in the year due to strong surface stratification. Most profiles included in our study do not have such a surface mixed layer. Therefore, we also calculated an equivalent mixed layer depth h_{BD} or depth of the "buoyancy deficit" as described in Randelhoff et al. (2017), which is more adapted for describing a seasonal freshening and continuous vertical density structure. The h_{BD} shoals when the seasonal stratification increases, and it defines the area where mixing is possible. For this study, the h_{BD} was derived with a density reference at a depth of 50 m (see Randelhoff et al., 2017) based on the MLD found in late April.

Vertical profiles of water column turbulence were measured on 23 June 2016 during a 13-h period. We used a self-contained autonomous microprofiler (SCAMP, Precision Measurement Engineering, California, U.S.A.) falling freely at roughly 0.1 m s^{-1} down to a maximum depth of 100 m. The dissipation rate of turbulent kinetic energy (ε) was obtained from fitting the theoretical Batchelor spectrum to the SCAMP inferred microstructure temperature gradient spectrum using the modified maximum likelihood method from Ruddick et al. (2000) over 1-m deep segments. More details about the method can be found in Cuypers et al. (2012). The diapycnal diffusivity (K_z) was parameterized as a function of turbulence intensity (buoyancy Reynolds number Re_b) for different turbulence regimes (Bouffard and Boegman, 2013). As opposed to the Osborn (1980) formulation, which uses a constant mixing efficiency that overestimates K_z at high Re_b, this parameterization accounts for the variability in the mixing efficiency depending on the intensity of the turbulence.

2.4. Nutrients and chlorophyll a

To measure inorganic nutrients, nitrate (NO_3^-), nitrite (NO_2^-), phosphate (PO_4^{3-}) and silicate ($Si(OH)_4$), seawater and melted sea ice samples were filtered through GF/F filters and poured into 20-mL sterile polyethylene flasks. Thereafter, the samples were poisoned with 100 µL of mercuric chloride (600 mg per 100 ml) and stored in the dark until analyses in the laboratory using an automated colorimetric procedure (Aminot and Kerouel, 2007). A nitracline depth was defined as the shallowest depth where NO_3^- concentration exceeded 1 µM, based on depth-interpolated profiles of NO_3^- concentrations.

Every second day, seawater samples were collected through the 1-m^2 hole under the tent at eight depths (among the ice-water interface, 1.5, 5, 10, 20, 40, 60, and 75 m) using Niskin bottles. The concentrations of total chlorophyll *a* (TChl*a*, the sum of chlorophyll *a*, divinyl-chlorophyll *a* and chlorophyllide *a*) in seawater ($TChla_w$) and melted sea ice samples ($TChla_{0-3cm}$) were measured by high performance liquid chromatography (HPLC, Agilent Technologies 1200). Particle samples, collected on GF/F filters, were kept frozen at –80°C until analysis in the laboratory, as per the protocol described by Ras et al. (2008). Fluorescence profiles, a proxy of chlorophyll *a* concentration, were also estimated with a CTD-mounted chlorophyll *a* fluorometer down to 350 m (Wetlabs ECO-FLRT s/n FLRT-3385).

3. Results

3.1. Weather conditions

The late autumn/early winter (October to December) of 2014–2015 was slightly warmer than the same period in 2015–2016 (Figure S5A, Qikiqtarjuaq airport). In December 2014, the monthly average air temperature was about –20°C, while it was –24°C in December 2015, a month of intense sea ice formation. In both years, strong winds were observed in late autumn. For example, a daily averaged wind speed exceeding 15 km h^{-1} persisted over nine consecutive days between 9 and 17 November 2014. The following year, a storm was detected with a rather short duration of 3 days (24–26 December 2015), but stronger intensity with a daily averaged wind speed of 37 km h^{-1} (red vertical lines, Figure S5B).

During the winter (from January to March), temperatures were lower in 2015 than in 2016, with a monthly mean air temperature minimum of –36°C in February 2015 compared to –28°C in February 2016. The winter in 2015 was one of the coldest of the last 35 years for northern Canada (Figure S6). Weather conditions prior to the field campaigns (from the freezing onset in November to April) were also different in terms of total precipitation (in equivalent water) with values 5 times lower in 2014–2015 compared to 2015–2016 (6.3 mm and 34.2 mm, respectively) (Figure S5D).

At the end of April, the air temperature was lower in 2015 compared to 2016 (–15°C and –10°C respectively; **Figure 2A**); the year 2016 also experienced warm events (>0°C) in early May. Sea ice thickness was about 1.2 m in both years, but the snow cover was initially thinner in 2015 than in 2016 (~20 cm and 40 cm, respectively; **Figure 2D**). However, more snowfall events occurred in mid-May 2015 compared to the same time period in 2016 (Figure S5D) leading to a thicker snow layer (~40 cm and 30 cm, respectively).

By the end of May, snow/ice thickness ranged around 15–40 cm/110–135 cm in 2015 and 20–50 cm/115–150 cm in 2016 (**Figure 2D**). Sea ice was much colder and saltier in May 2015, with ice temperatures below –3°C (**Figure 3A**) and bulk salinity reaching 12 throughout most of the ice thickness (**Figure 3B**) compared to barely –1.5°C and 6, respectively, in May 2016. In 2015, the sea ice started to warm and freshen slightly after the air temperature first reached 0°C, as well as during the rest of the snow melt period (**Figures 2A, 3A**). In comparison, in 2016, bulk salinity was very low and homogeneous from May to July, and the ice temperature increased as soon as the air temperature hit 0°C. In May 2015, the brine volume was about 50% greater than that observed in 2016 (vertical average of 15% and 10%, respectively; **Figure 3C**). During both years, the seasonal variation of the depth-averaged brine volume in the sea ice increased with time (**Figure 3C**) ranging from about 6 to 35% in 2015 and from 7 to 25% in 2016. The proportion of brine volume in the bottom 10 cm of the sea ice cores was twice as high in 2015 as in 2016 (24.4 ± 8.5% and 12 ± 3.1%, respectively; significantly different: *t*-test, *p*-value = 1.9×10^{-9}).

3.2. Light transmission

Light transmittance through the snow and sea ice covers differed between the two years (**Figures 2E**, S8). At the beginning of May 2015, about twice as much light was transmitted as at the same time in 2016. Later on, the situation reversed. Under-ice PAR at 1.3 m (*PAR(1.3m)*) decreased by a factor of 3.6 in 2015 (0.12 to about 0.033 mol photons m^{-2} d^{-1}), while it increased by a factor of 3.2 in 2016 (0.05 to about 0.16 mol photons m^{-2} d^{-1}). By the end of May, *PAR(1.3m)* was on average three times higher in 2016 compared to 2015.

In 2015, the snow thickness started to decrease and the temperature rose above 0°C five days later than in 2016 (8 and 3 June, respectively; **Figure 2A, D**). These dates marked the snow melt onset (**Figure 2D**). During the snow melt period (~2 weeks), *PAR(1.3m)* increased significantly by about a factor of 10 in 2015 (from 0.1 to 1 mol photons m^{-2} d^{-1}) and by a factor of 17 in 2016 (from 0.2 to 3.4 mol photons m^{-2} d^{-1}). *PAR(1.3m)* started exceeding the 0.415 mol photons m^{-2} d^{-1} threshold one week after the onset of the snow melt in both years (**Figure 2E**). Once the snow depth was <10 cm, i.e., in an advanced melting stage, melt ponds started to form on 22 June 2015 and 15 June 2016 (**Figure 2D**). The melt ponds appeared concomitantly with further warming and freshening of the sea ice (**Figure 3**). During this melt pond period, *PAR(1.3m)* continued to increase and reached values three times higher (from 1 to 3.4 mol photons m^{-2} d^{-1} in 2015 and from 3.6 to 10 mol photons m^{-2} d^{-1} in 2016). By mid-July, *PAR(1.3m)* had increased by about three orders of magnitude from late April.

PAR(0$^+$) (atmospheric reference above sea ice) decreased by a factor of two (from 62 to 29 mol photons m^{-2} d^{-1})

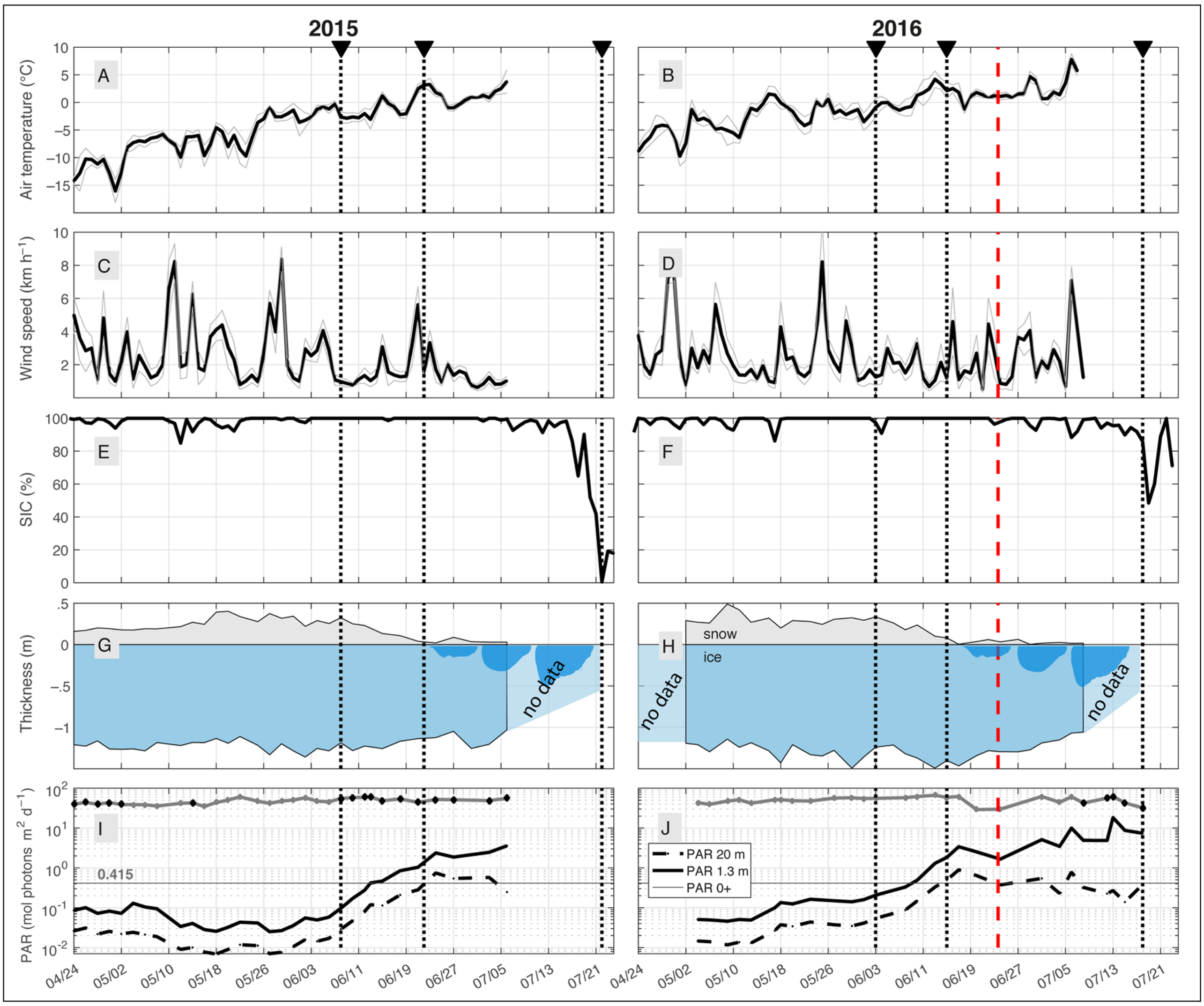

Figure 2: Temporal evolution of the environmental conditions in the air-snow-ice-ocean system. Time series of daily averaged environmental conditions for 2015 (left) and 2016 (right) of **A, B:** air temperature (°C) and **C, D:** wind speed (km h^{-1}) from the meteorological station with standard deviation in gray; **E, F:** remotely sensed sea ice concentration (%) from the AMSR-2 satellite; **G, H:** in situ snow and sea ice thickness (m), with melt ponds qualitatively illustrated in deep blue; **I, J:** in situ *PAR(0⁺)* above surface in gray with modeled values in black dots, underwater PAR at 1.3 m in black solid line, and at 20 m in dashed black line. Horizontal thin lines represent the 0.415 isolume thresholds from Letelier et al. (2004). Data in G, H, I and J are collected at the center of the sampling circle of 1.2-km radius every 2–3 days. Vertical dotted lines with triangle indicators on top chronologically represent snow melt initiation, melt pond initiation and sea ice breakup. The red dashed line indicates the date when turbulence was measured over a 13-h period. Dates are month/day. DOI: https://doi.org/10.1525/elementa.372.f2

due to increasing cloudiness from 19 to 25 June 2016. The same factor of two applied to *PAR(1.3m)* underneath the sea ice (3.4 to 1.6 mol photons m^{-2} d^{-1}). In 2015, PAR measurements were not conducted until the ice breakup (22 July 2015), but the 2016 field study shows that *PAR(1.3m)* reached values (18 mol photons m^{-2} d^{-1}), of about the same order of magnitude as the above surface *PAR(0⁺)* (~55 mol photons m^{-2} d^{-1}) just before the breakup on 18 July 2016. In contrast, *PAR(20m)* decreased by a factor of three in 2015 and seven in 2016 during the melt pond period until the ice breakup.

3.3. Water masses and currents

The conservative temperature-absolute salinity diagram (**Figure 4**) and the ANP relationship (Figure S3) allowed us to update the estimates found in the literature (i.e., Tang et al., 2004). We offer these precise definitions of water masses observed at the study site and for the closest sampled station during the 2016 CCGS *Amundsen* campaign in the same period (see station 403 in **Figure 1**):

1. **Atlantic Waters (AW).** These waters are more specifically an Atlantic-derived water mass (**Figure 4**) defined by a conservative temperature Θ > 1°C and absolute salinity $S_A > 34$ (g kg^{-1}), because they are colder and fresher than original Atlantic waters. AW were found generally deeper than 300 m, and only partially captured in 2016. Samples at depth at the study site were actually thermocline water, and nutrient sampling did not extend deeply enough to characterize ANP for this water mass. However, offshore measurements made in 2016 from the CCGS

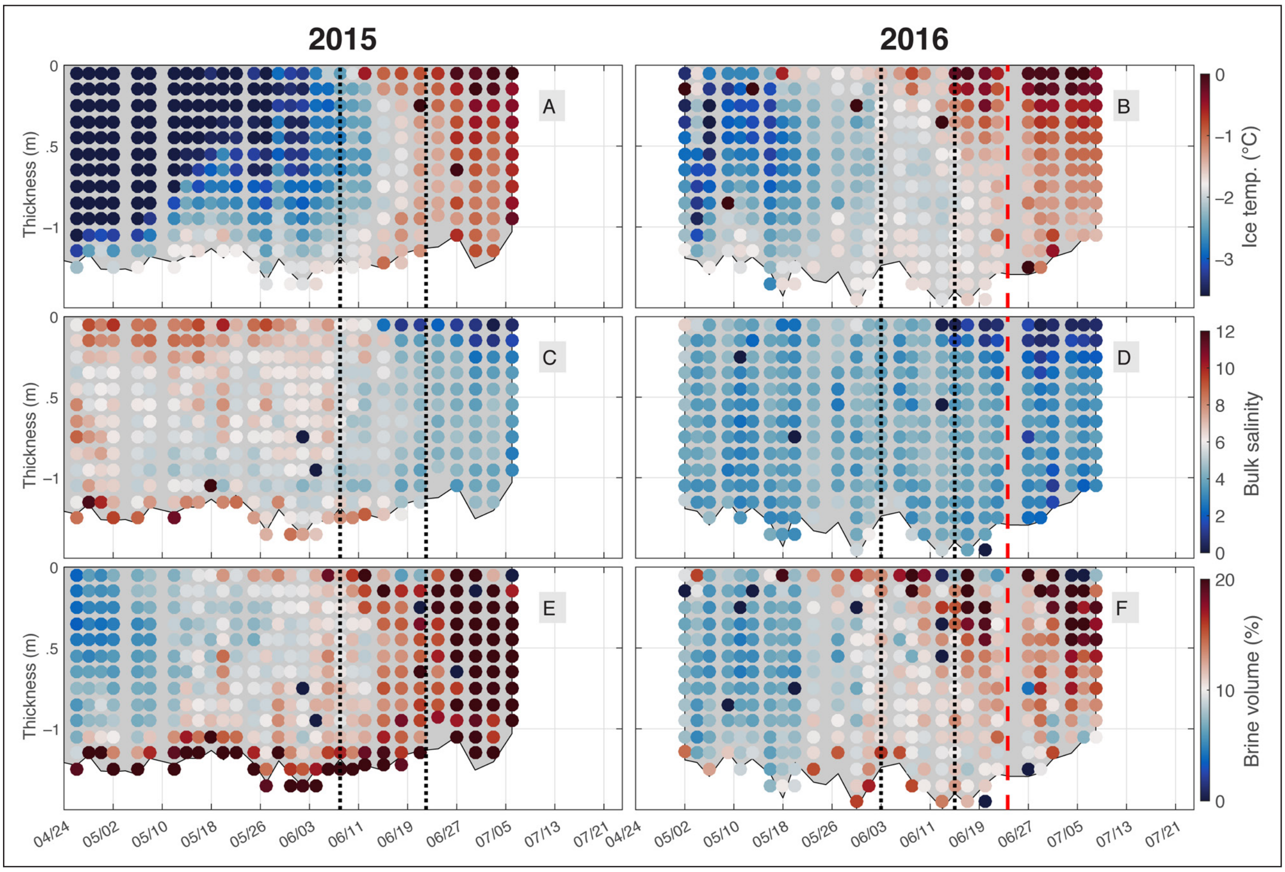

Figure 3: Temporal evolution of sea ice properties. Time series for 2015 (left) and 2016 (right) of **A, B:** sea ice temperature; **C, D:** bulk salinity; and **E, F:** brine volumes as a function of depth (with sea ice thickness in light grey background). Vertical dotted lines chronologically represent snow melt initiation and melt pond initiation. The red dashed line indicates the date when turbulence was measured over a 13-h period. Dates are month/day. DOI: https://doi.org/10.1525/elementa.372.f3

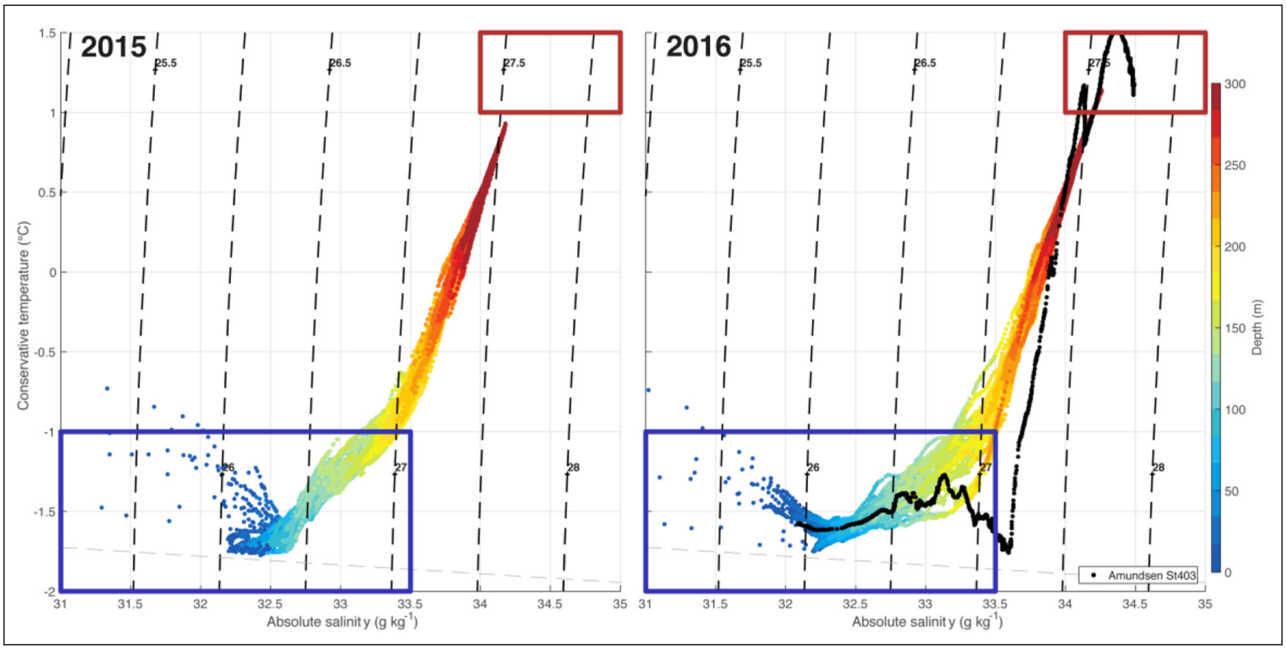

Figure 4: Water masses determined from salinity, temperature and depth. Conservative temperature (°C) versus absolute salinity (g kg^{-1}) diagrams for all CTD profiles collected during both 2015 (left) and 2016 (right) field campaigns. Points are colored according to depth. In 2016, the closest station (station 403; see the green cross in Figure 1) sampled by the CCGS *Amundsen* off the continental shelf in the Baffin Bay basin is in black. The blue box defines the Arctic Waters (AW), and the red box marks the Atlantic Waters (ArW). DOI: https://doi.org/10.1525/elementa.372.f4

Amundsen research icebreaker showed ANP ≤ 0.1 (Randelhoff et al., 2019). In the literature, this water mass has also been referred to as West Greenland Intermediate Waters, West Greenland Current Water or Baffin Bay Intermediate Water (Tang et al., 2004; Münchow et al., 2015).

2. **Arctic Waters (ArW).** These waters are defined by $\Theta < -1$°C and $S_A < 33.5$ g kg^{-1} (**Figure 4**). ArW were the main water masses found at the study site. The range of ArW ANP was 0.4–0.6 from April to June 2015, and 0.6–0.8 during the same time period in 2016. The average was 0.51 in 2015, and increased to 0.62 in 2016. These ArW ANP values are higher than those reported offshore from the CCGS *Amundsen* cruise (Randelhoff et al., 2019).
3. **Surface Meltwaters.** These waters form from ice melt in spring. They remain mainly near the surface and increase in temperature due to contact with the atmosphere and radiative heating, which leads to a very wide range of temperature and salinity. However, they are generally fresher and warmer than the ArW.

The surface signature of the ArW in the top 150 m remained very similar to that of Station 403 of the CCGS *Amundsen* station grid (**Figure 4**), which suggests that the study site is representative of offshore sites in terms of hydrography.

In late April, before summer stratification, the MLD was about 55 and 58 m deep for 2015 and 2016, respectively (Figure S4). The depth of the MLD coincided well with the depth of the winter overturning (i.e., the depth of the minimum temperature; **Figure 4**) which ranged from ~ 40 m in 2015 to 70 m in 2016. In both years, the melt pond onset coincided with a decrease in surface salinity in the first 5 m (from 32.5 to 28 g kg^{-1} in 2015 and from 32.2 to 30.6 g kg^{-1} in 2016; **Figure 5C**) and an increase in the surface temperature (from –1.6 to –0.45 °C in 2015 and from –1.6 to –0.9°C in 2016; **Figure 5B**).

Whereas in winter the water column was stratified only by salinity gradients (Turner angle < –45°; Figure S9), the melt pond period was always characterized by a combined effect of temperature and salinity on stratification (–45° < Turner angle < 0°; Figure S9). Increases in meltwater and solar radiation made the surface water both fresher and

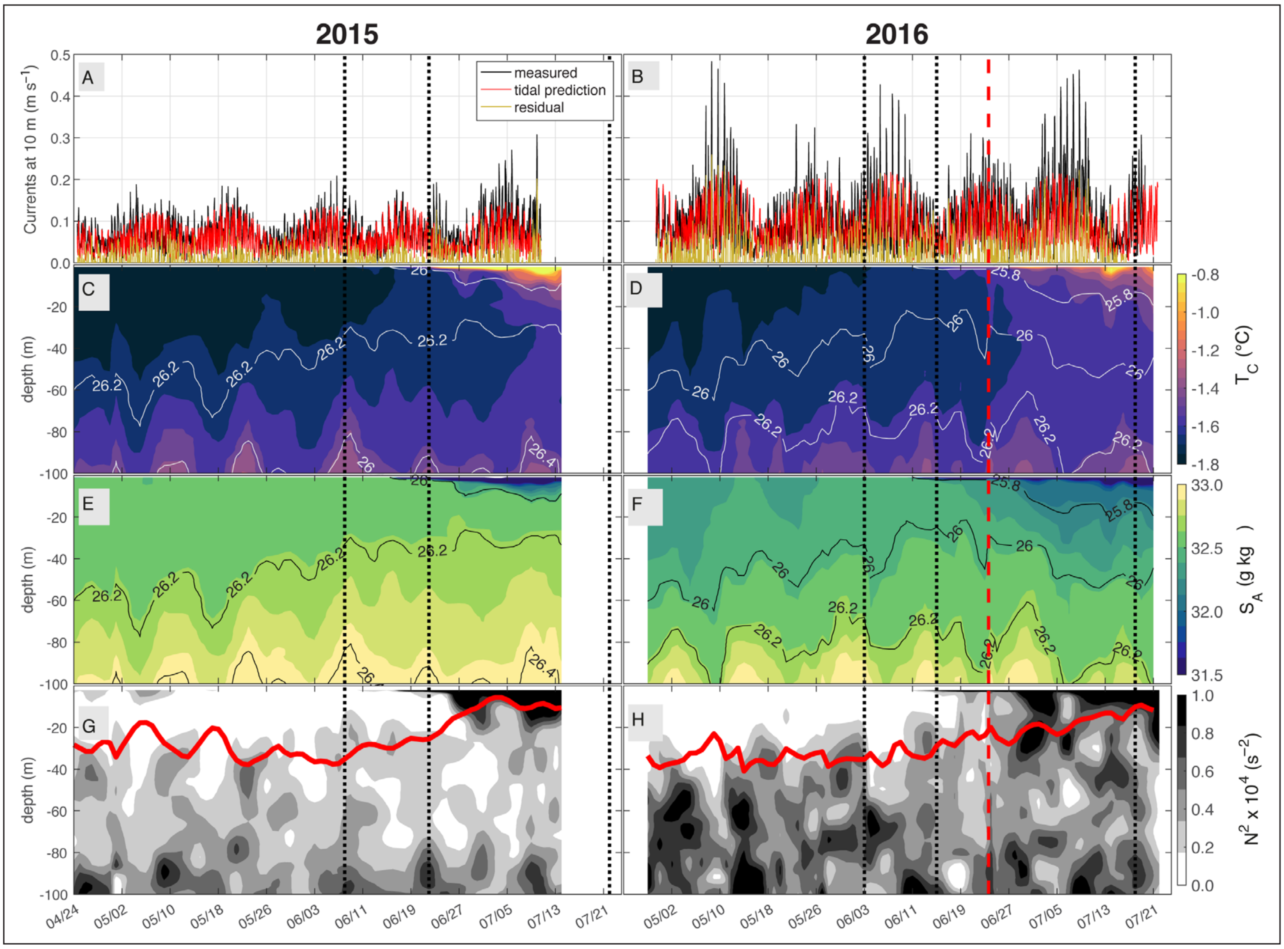

Figure 5: Hydrographic temporal evolution of the water column. Time series for the years 2015 (left) and 2016 (right) of **A, B:** in situ absolute current velocities at 10-m depth in black and predicted from a harmonic analysis in red; **C, D:** conservative temperature Θ (°C) and **E, F:** absolute salinity S_A (g kg^{-1}) fields (color bars), with superimposed isopycnals of potential density anomaly lines; and **G, H:** Brunt–Väisälä frequency N^2 (s^{-2}) (gray-scale bar) with the h_{BD} is in red line. Vertical dotted lines chronologically represent snow melt initiation, melt pond initiation and sea ice breakup. The red dashed line indicates the date when turbulence was measured over a 13-h period. Dates are month/day. DOI: https://doi.org/10.1525/elementa.372.f5

warmer, which increased surface stratification by a factor of 10 (Brunt-Väisälä frequency 10 m $N^2 \geq 10^{-4}$ s^{-2} against values of $\leq 10^{-5}$ s^{-2} before the melt pond onset, 1.5–5 m) in early July (**Figure 5D**). The meltwater accumulation is also illustrated by the shoaling of the h_{BD} from 25–30 m to about 5–20 m (**Figure 5D**).

This association between sea ice melt and upper ocean stratification seemed to be timed with maximal current speed fields in early July in both years. This timing corresponded to a spring tide cycle (**Figure 5A**) with maximum current velocities of about 0.25 m s^{-1} in 2015 and 0.45 m s^{-1} in 2016 recorded between 3 and 11 July. This period also corresponded to maximum mean current speed (~0.12 m s^{-1} in 2015; ~0.2 m s^{-1} in 2016; **Figure 6A**) concomitant with a local isopycnal deepening. The daily mean kinetic energy (KE = 1/2 [$u^2 + v^2$], at 10 m) was 3–5 times higher on average during the spring tides compared to the neap tides (~55 cm^2 s^{-2} vs $\leq$ 15 cm^2 s^{-2} in 2015 and ~150 cm^2 s^{-2} vs $\leq$ 30 cm^2 s^{-2} in 2016).

The water-column profiles of temperature, salinity and density were highly modulated by this spring-neap tidal cycle, resulting in periodic shoaling and deepening of isolines (**Figure 5**; see Figure S9 for the entire water-column profile). The amplitude of the isopycnal oscillations reached several tens of meters (~20–30 m) indicating important baroclinic motions. The semi-diurnal signal was aliased by the daily sampling so that the observed spring tide amplitude lagged and was always weaker than the real one, but the apparent periodicity is equal to the spring-neap cycle modulation duration (~4 days). We used a harmonic analysis (Pawlowicz et al., 2002) to derive predicted tides on each valid bin (from 10 to 40 m). As expected, the tide was found to be the main driver of local currents explaining about 70% of their variance, and it was dominated by the semi-diurnal component M2 (Figure S10). The predicted tidal currents correlated significantly with the total observed ones (r = 0.60, $p < 10^{-4}$), but the prediction underestimated the magnitude of the tidal component of the observed current. The tidal current appears to have about the same direction and magnitude between 10 m and 40 m (Figure S11), and was roughly aligned with the 350-m isobath (**Figure 1**). The amplitude of the tidal currents was about half as large in 2015 than in 2016, which is more likely to happen with baroclinic currents that are very sensitive to stratification. Modelled tidal currents from a 2-D barotropic model (WEBTIDE v0.7.1; Collins et al. 2011) gave similar results (spring tide velocity ~ 4 cm s^{-1}) for both 2015 and 2016.

We also recorded a residual signal (total measured – tidal prediction – mean current) with a 12.5-h period. This signal may be typical of internal waves, especially when measured on the shelf break of a narrow fjord, where a tidal signal may be modulated on a M2 period (Morozov and Paka, 2010) and result in an isopycnal oscillation such as the one observed at the study site. The rest of the signal can be attributed to a weak mean current (**Figure 6**). Averaged over the whole time series, the intensity of the mean current peaked at 0.06 m s^{-1} in 2015 and at 0.1 m s^{-1} in 2016 with respective averages of about 0.03 m s^{-1} and 0.045 m s^{-1}. In 2015, the velocity field pointed East in 2015 from late April until mid-May. It then shifted North, and finally, after mid-June, it pointed West (in-fjord). In 2016, the velocity field was much more stable, almost constantly facing West.

3.4. Mixing and turbulence over one M2 tidal cycle (13 h)

The median profile of the rate of dissipation of turbulent kinetic energy (ε) over the entire 13-h deployment period shows a 20–25 m thick top layer of elevated dissipation

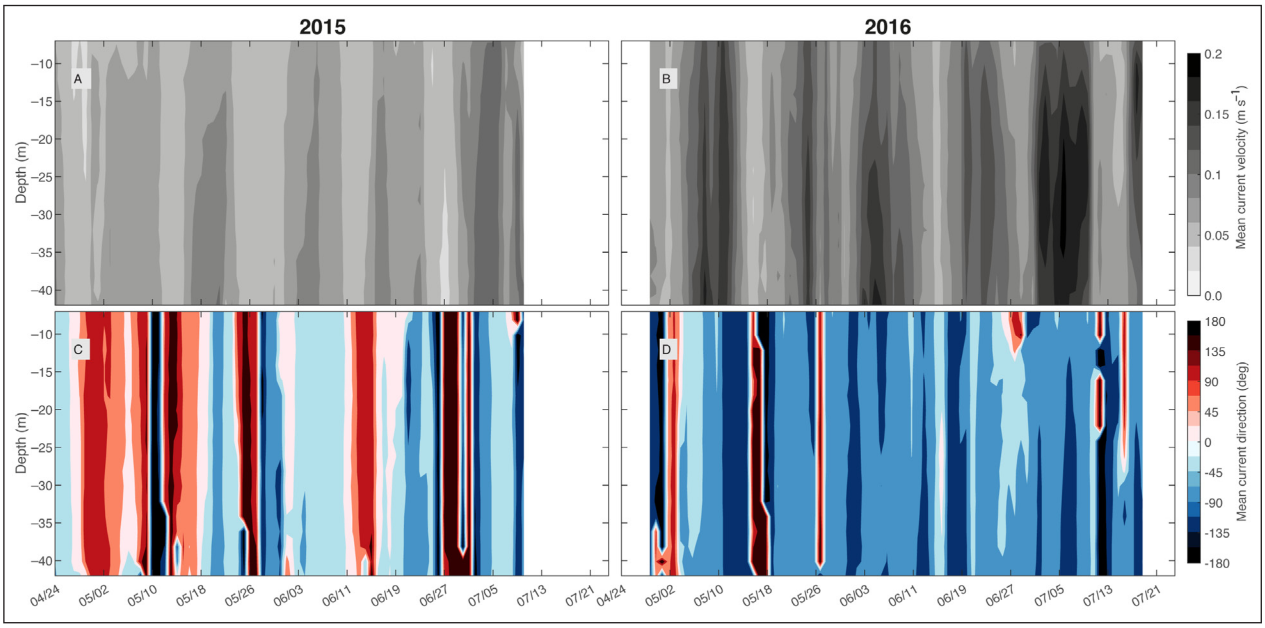

Figure 6: Temporal evolution of the mean ocean current profiles. Time series for 2015 (left) and 2016 (right) of daily mean of **A, B:** current velocity (m s^{-1}, grey-scale bar); and **C, D:** current direction (0° = northward, color bar). Red indicates an out-fjord/eastward direction, while blue represents an in-fjord/westward direction. Dates are month/day. DOI: https://doi.org/10.1525/elementa.372.f6

rate with values above 10^{-8} W kg^{-1} (**Figure 7**). Deeper, in the more stratified layer, an alternation of low and high ε was observed, suggesting internal wave-breaking events.

An overview of the ε profiles over the 13-h high-frequency sampling period reveals that higher dissipation occurred during the first half of the sampling period when currents were stronger (**Figure 8**). As the tides dominate the current and the SCAMP sampling was taken at spring tide, spanning a complete tidal cycle, we assume that the mean dissipation rate in **Figure 7** is representative of an upper bound for the 2016 period during an early stratification stage. Dissipation was likely lower in 2015 due to weaker currents.

The mean (time-averaged over the 13-h period) mixing coefficient K_z, also called turbulent or eddy diffusivity, indicates the capability of the flow to mix tracers like heat, salt, nutrients, or algae. K_z reveals a complex vertical structure. A very thin ice meltwater layer had started to form a few days prior to the SCAMP deployment, and it drove a marked reduction in K_z in the first few meters because strong stratification inhibits vertical mixing. Nonetheless, K_z was more elevated in the mixing layer (3.4×10^{-4} m^2 s^{-1}) and weaker below (2.1×10^{-4} m^2 s^{-1}). Therefore, a parcel located in the mixing layer could be vertically mixed and transported over a length scale of about 1.2 m every day, simply based on the dimensional argument that diffusivity

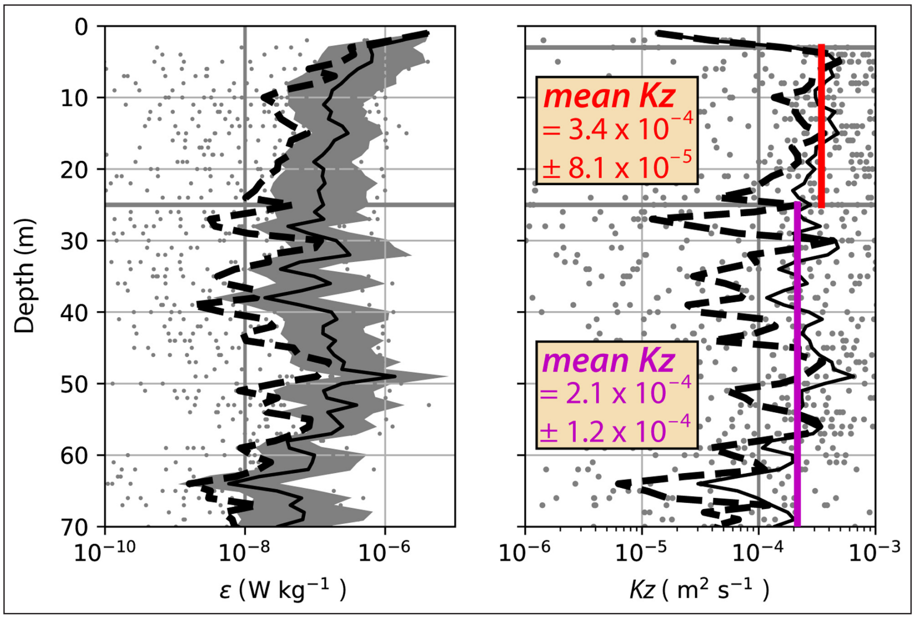

Figure 7: Averaged turbulence profile during a tidal cycle. Time-averaged mean (thin, solid) and median (thick, dashed) dissipation rate of turbulent kinetic energy (ε) on the left and time-averaged mean (thin, solid) and median (thick, dashed) vertical turbulent diffusivity (K_z) on the right, sampled using the SCAMP during a 13-h period over a tidal cycle in 2016. The grey shading indicates the 95% confidence limits (calculated as $\|\varepsilon\| \pm 1.96\sigma/\sqrt{n}$, where *s* is the standard deviation of the log-transformed data and *n* is the number of samples in each bin) and the grey dots are all data points. Insets in the right panel provide the mean K_z as arithmetic means of the overall data points in the two indicated depth intervals, plus/minus one standard deviation. DOI: https://doi.org/10.1525/elementa.372.f7

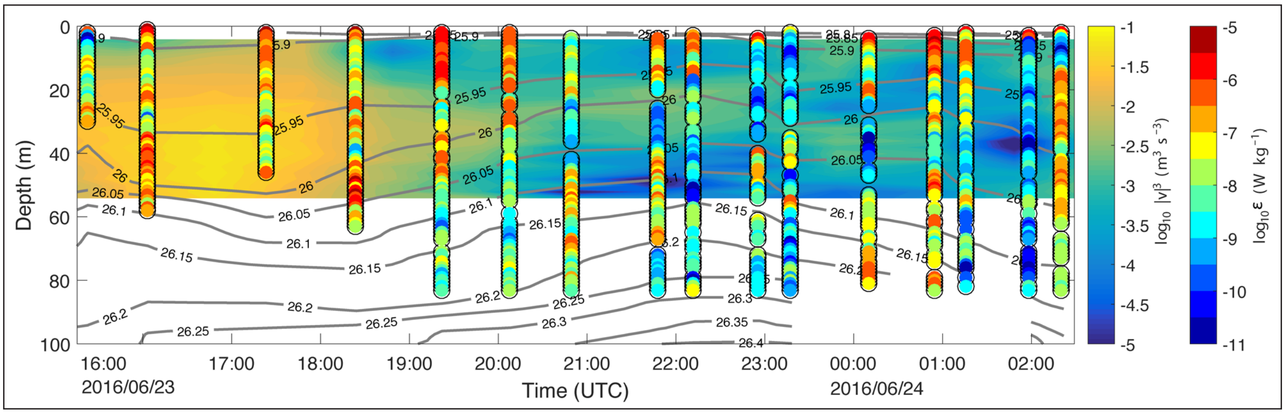

Figure 8: Turbulence modulation during a tidal cycle. The 13-h period documenting the cubed current speed (m^3 s^{-3}, background field, inner color bar), and the dissipation rate of turbulent kinetic energy (W kg^{-1}, scatter points, outer color bar) with superimposed isopycnals of the potential density anomaly (kg m^{-3}) during a tidal cycle. Date is year/month/day. DOI: https://doi.org/10.1525/elementa.372.f8

is a length scale squared divided by a timescale ($K_z = H^2/dt$). This number falls to 0.7 m d^{-1} below the mixing layer.

Note that the values measured by the SCAMP below the thin meltwater layer are representative of well-mixed conditions in the upper 20 m (see **Figure 5D**). Following the SCAMP deployment, the upper 20 m progressively re-stratified and we expect K_z to decrease there.

3.5. Inorganic nutrients and algal biomass

The bulk concentration of nitrate + nitrite in the bottom 10-cm segments of the sea ice, $[NO_3^- + NO_2^-]_{0\text{–}10cm}$, differed between the two years (**Figure 9B**). In 2015, $[NO_3^- + NO_2^-]_{0\text{–}10cm}$ increased from 1–9 µmol L^{-1} to almost 30 µmol L^{-1}, then collapsed to ~0 µmol L^{-1} three days after snow melt onset (8 June). In 2016, $[NO_3^- + NO_2^-]_{0\text{–}10cm}$ was much lower, starting at 3–5 µmol L^{-1} in early May, then continuously decreasing until depletion on 27 June. Integrated biomass in the bottom 0–3 cm of the sea ice, TChl$a_{0\text{–}3cm}$, slightly increased until reaching a maximum just before the snow melt onset (26 mg m^{-2} on 27 May 2015; 6 mg m^{-2} on 30 May 2016; **Figure 9C**). After the snow melt onset, TChl$a_{0\text{–}3cm}$ decreased to values less than 10 mg m^{-2} in 2015 and less than 2 mg m^{-2} in 2016. Overall, the averaged sea ice algal biomass was about four times lower in 2016 (1.95 ± 1.45 mg m^{-2}) than in 2015 (8.33 ± 5.88 mg m^{-2}).

Following the same pattern as that of TChl$a_{0\text{–}3cm}$, nitrate+nitrite concentration $[NO_3^- + NO_2^-]$ in the surface layer of the water column (see $[PO_4^{3-}]$ and $[Si(OH)_4]$ in Figure S12) increased slightly until reaching a maximum just before snow melt onset (5.4 µmol L^{-1} in 2015 and 5.2 µmol L^{-1} in 2016 at 1.5 m; **Figure 9D**). The water-column integrated biomass TChla_w (**Figure 9C**) was negatively correlated with ice algal TChl$a_{0\text{–}3cm}$ (r = –0.54, p = 10^{-3} in 2015; r = –0.60, p = 8 10^{-4} in 2016) and with $[NO_3^- + NO_2^-]$ (r = –0.91 in 2015; r = –0.84 in 2016, at 5 m, $p <$ 10^{-4}). For example, TChla_w decreased locally between 27 May and 3 June 2015 while TChl$a_{0\text{–}3cm}$ increased. In contrast, TChla_w increased as soon as TChl$a_{0\text{–}3cm}$ decreased in early June in both years. After melt pond onset, TChla_w rapidly increased to reach a similar maximum in both years: about 152 mg m^{-2} on 12 July 2015 and 182 mg m^{-2} on the same date in 2016. Nutrients also decreased faster, and were almost completely depleted by 10 July 2016 in the surface layer. While nutrients were also depleted at depth in 2016, $[NO_3^- + NO_2^-]$ remained almost unchanged at 40 m deep (~5 µmol L^{-1}) in 2015. The average under-ice

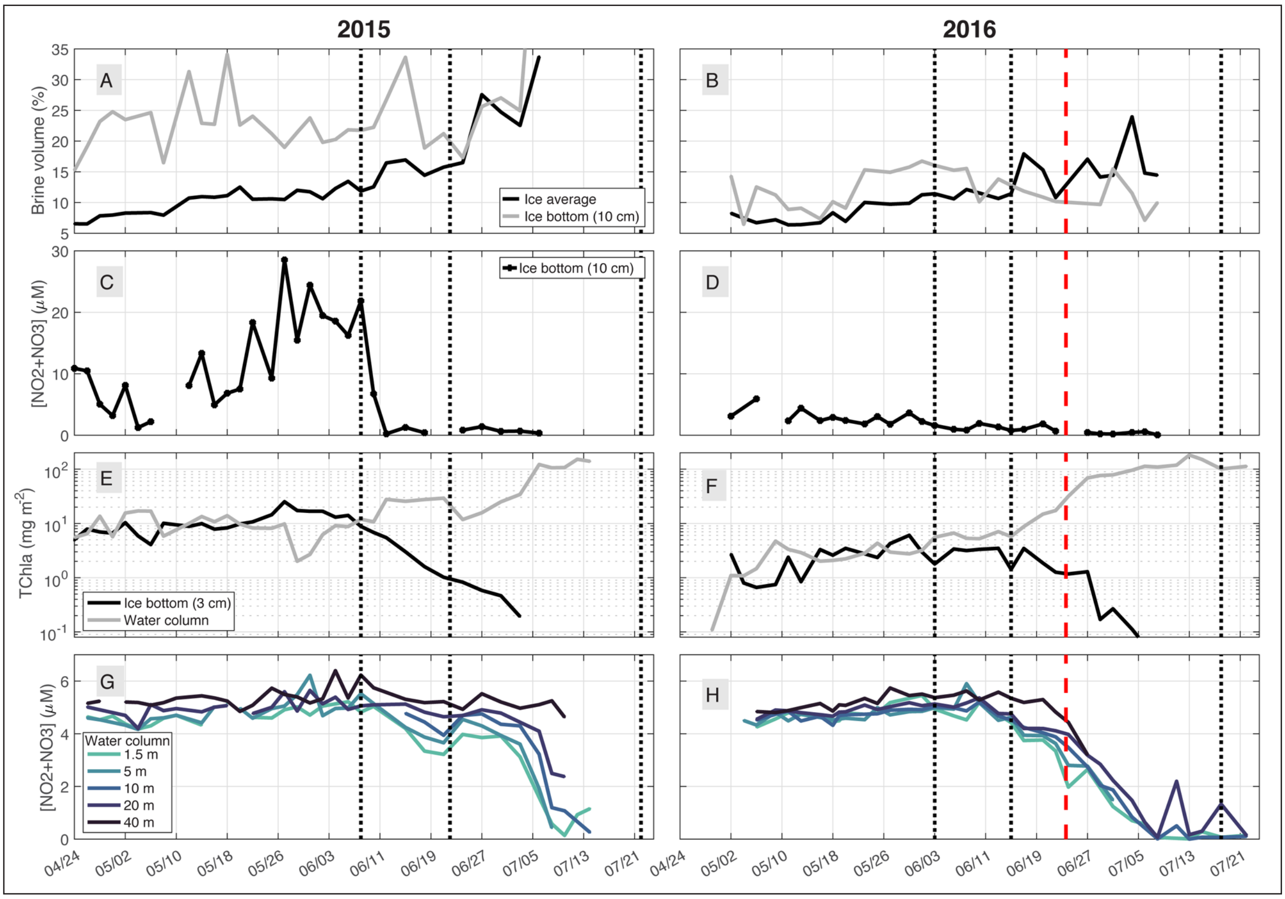

Figure 9: Temporal evolution of biogeochemical properties in sea ice and seawater. Time series for 2015 (left) and 2016 (right) of **A, B:** depth-averaged and bottom sea ice brine volumes; **C, D:** nitrate and nitrite concentration $[NO_3^-+NO_2^-]$ in the bottom 0–10 cm of the sea ice; **E, F:** integrated TChl$a_{0\text{–}3cm}$ concentration in the bottom 0–3 cm of the sea ice in black and in the water column in gray (note the log scale); and **G, H:** $[NO_3^-+NO_2^-]$ in the water column at several depths. Vertical dotted lines chronologically represent snow melt initiation, melt pond initiation and sea ice breakup. The red dashed line indicates the date when turbulence was measured over a 13-h period. Dates are month/day. DOI: https://doi.org/10.1525/elementa.372.f9

phytoplankton biomass was similar in both years when derived over the same period (30.4 ± 41.4 mg m^{-2} in 2015 and 37.6 ± 52.0 mg m^{-2} in 2016, between 27 April and 14 July).

Water column TChla_w was depth-integrated down to the deepest measurement, but the resulting values could be underestimates, as non-negligible [TChla_w] could exist at greater depth where no measurements were available. Using smoothed [TChla_w] profiles (a 5-point running median filter followed by a 7-point running mean filter) measured with the fluorometer, we were able to quantify this underestimation: it ranged from 5 to 60% in 2015 and from 2 to 50% in 2016 (Figure S13). On average, depth-integrated TChla_w was underestimated by 28% in 2015 and by 18% in 2016. The high underestimate of 60% was found on 2 May 2015, and 50% on the same date in 2016, but these underestimations only affect profiles with very low TChla_w (6 mg m^{-2} and 2.5 mg m^{-2}, respectively).

4. Discussion

4.1. Ocean dynamics

4.1.1. Advection

The study site was representative of the upper open ocean of western Baffin Bay in terms of water masses (Tang et al., 2004; Curry et al., 2014; Randelhoff et al., 2019), which are strongly influenced by ArW flowing southward from the northern passages (from North to South: Nares, Jones, and Lancaster straits with respective sills about 250, 120 and 125 m deep; see **Figure 1** in Wu et al., 2012) and carrying with them a Pacific-origin signature (Tremblay et al., 2015). This fresh, cold ArW mass meets and overlies the re-circulating AW from the West Greenland Current that have been thoroughly modified and altered since their departure from the North Atlantic. The Pacific influence seems to have been more pronounced in 2016 (higher ANP values), and may be responsible for the greater subsurface stratification (40 m and below). The ArW generally carry their strong stratification throughout the winter (i.e., they are rarely homogenized), as evidenced by strong subsurface stratification long before the onset of the melt period at depth (100–200 m; Figure S9). The increased subsurface stratification and mean currents in 2016 appear to be linked through the large-scale circulation in Baffin Bay (Figure S14).

To understand whether the phytoplankton biomass observed at the study site (here dominated by diatoms; P-L Grondin, personal communication) may have been produced beyond the ice edge in open waters and then transported to the study site, we can consider the following simple calculations. A maximum mean velocity of about 0.045 m s^{-1} means that water from the ice edge, which was located more than 200 km away before July of both years (Figure S15), would have been in transit for a minimum of 52 d to reach the study site. In early July, the distance from the ice edge to the study site decreased to less than 100 km decreasing by a factor of two the minimum travel time needed for a water parcel to move from one place to the other. Therefore, with a typical diatom sinking rate of 1 m d^{-1} (Riebesell, 1989), a diatom cell located at the ice edge before July would sink to a depth of >52 m by the time it arrived at the sampling site. Following the same calculations in early July, a diatom cell would have sunk by at least 26 m, and therefore out of the mixing layer. However, we suspect the downward sinking would be much greater because the calculation assumes a spatially uniform, maximum and linear current extending all the way from the ice edge in the basin into the fjord, a rather unrealistic condition. At the study site, most phytoplankton biomass was found above 30 m. In other words, our back-of-the-envelope calculations serve to show that our measurements at the study site were not subject to a highly advective regime and that the observed under-ice phytoplankton bloom is produced locally.

4.1.2. Tides and mixing

Using a harmonic analysis, we showed that current velocities were dominated largely by tides. This idea was further corroborated by the tidal modulation of the dissipation of turbulent kinetic energy and isopycnal depths. A parcel located at the study site was likely to move around a perimeter of 1 to 2.7 km, oscillating on a M2 tidal cycle period (12.42 h, averaged velocities = 0.045–0.12 m s^{-1}). While the stronger mean current in 2016 may have been influenced by a large-scale circulation intensification, the stronger tides were probably due to a constructive interference between tidal components and/or variations in the internal wave field (sensitive to stratification; e.g., Morozov and Paka, 2010). Our data set does not give us the means to solve this puzzle; we assume resolving it would necessitate large-scale modelling of Baffin Bay hydrography and currents. In any case, the year 2016 was more energetic with faster mean, tidal and residual currents velocities. We suggest that the spring-tidal energy, in particular, may have contributed to the deepening of the surface stratified layer by mixing the melt layer with the underlying ArW to about 25 m in 2016. This layer corresponded to the mixing layer, where active turbulent mixing occurred as a result of surface processes leading to the injection of turbulent kinetic energy (Brainerd and Michael, 1995). The more energetic currents in 2016 (faster mean, tidal and residual currents velocities) led to deeper mixing as illustrated by the deeper meltwater distribution starting in late June 2016 (**Figure 5**). In contrast, in 2015 the meltwater layer was shallower and its freshening and warming were more abrupt and intense. If the stronger sub-surface stratification in 2016 presumably led to reduced vertical mixing below 40 m, in the ice-ocean boundary itself, the stronger currents must have led to greater shear at the surface, producing even more vertical mixing.

During strong mixing conditions (i.e., spring tidal cycle in the mixing layer, K_z = 3.4 10^{-4} m^2 s^{-1}, H (mixing layer depth) = 20 m), the turbulent mixing timescale would be about 1 d ($T_{min} = H^2/K_z$ = 21.3 h) which is about the same order of magnitude as phytoplankton photoacclimation (1–2 d; Cullen and Lewis, 1988) and cell division time (>1.6 d; Lacour et al., 2017; these estimations are based on algal culture under nutrient-replete conditions and may be overestimated when compared to field conditions).

During lower mixing conditions (i.e., neap tidal cycle), turbulent mixing remains on the same timescale but increased by 50% (T_{min} = 35 h ~ 1.5 d). Therefore, during spring tides, mixing occurs with a time scale equal to or shorter than photoacclimation and cell division time, and the mixing layer is homogenized. On the contrary, if the timescale for the response is shorter (which is likely during a neap tidal cycle), phytoplankton in a mixed layer may exhibit a vertical gradient associated with adaptation to ambient light intensities.

4.2. Sea ice history and brine volumes

Brine volumes were 50% larger in 2015 than in 2016. This difference was due mainly to large brine volumes at the bottom of the ice in 2015 (>20%), whereas 2016 vertical profiles were surprisingly almost homogeneous. Brine volume is basically a function of both sea ice bulk salinity and temperature (Petrich and Eicken, 2010, 2017), but a clear offset in bulk salinity was observed between the two years, as illustrated in Figure S16. In 2015, the bottom sea ice was about two times as saline, which explained the greater brine volume in the bottom part of the sea ice. Rapid growth results in more salt entrapment (Cox and Weeks, 1983). Therefore, brine volume (i.e., bulk salinity) differences may find an answer in sea ice thermodynamic history. Colder winter air temperatures, shorter freezing period, lower autumnal snowfall (less insulation) and colder sea ice temperatures are factors that all converge toward a possible faster ice growth rate in 2015 compared to 2016.

The thermodynamic growth of sea ice slows down, however, as the ice thickens, which results in bulk salinity increasing towards the top of the sea ice. The very low and homogeneous brine volumes observed in 2016 thus exclude the ice growth rate as the only explanation. A thin layer of dry snow laid over a thick layer of already wet snow (Verin et al., 2019) in 2016 by the time the camp was set up. The presence of wet snow indicated that episodic melt events had already occurred. The ice was also warmer (i.e., more permeable) than in 2015. Brine convection over the depth of the sea ice can yield significant desalination well before summer (Jardon et al., 2013), but lack of evidence about the sea ice history (i.e., winter sea ice sampling) hinders robust interpretation of brine volume in this study. Slower ice growth and more extensive brine drainage due to warmer ice, however, could explain the low bulk salinity observed that year. Ice algae, in response to a warming (Campbell et al., 2014) and desalination of the ice cover (Mundy et al., 2005), have been shown to slough from the ice bottom. Thus, an early drainage event could have caused a sloughing event of ice algal biomass prior to the commencement of our study in 2016, potentially influencing the low biomass accumulation observed in 2016.

4.3. The roles of clouds, snow, melt ponds and ice algae on light availability

Light availability below landfast sea ice is driven by the properties of 1) the incident light field that results from celestial mechanics, cloudiness, and cloud optical thickness; 2) sea ice surface conditions (e.g., snow, melt pond, white or bare ice); and 3) sea ice properties (e.g., thickness, brine volume, ice algae concentration) (Petrich and Eicken, 2017). Here we briefly discuss the relative contributions of cloud, snow and ice algae in driving under-ice light availability in 2015 and 2016.

The month of May 2015 provided an excellent case study for estimating the relative impacts of snow and ice algae on light availability. Indeed, we observed a decrease in transmittance at 1.3 m concomitantly with snowfalls (**Figure 2D, E**) and an increase in $\mathrm{TChl}a_{0-3\mathrm{cm}}$ (**Figure 8**). At the beginning of May 2015, before snow melt onset, sea ice transmittance was about 0.2%. By mid-May, snowfalls had added >10 cm to the snowpack, reducing the transmittance to a minimum of 0.06%. The new snow corresponded to a decrease in transmittance by a factor of 3.3, while $\mathrm{TChl}a_{0-3\mathrm{cm}}$ remained roughly constant around 6.9 ± 2.6 mg m^{-2}. Over the season, the transmittance was significantly negatively correlated with snow thickness ($r = -0.74$, $p < 10^{-4}$ in 2015; $r = -0.78$, $p < 10^{-4}$ in 2016).

By the end of May 2015, $\mathrm{TChl}a_{0-3\mathrm{cm}}$ increased from about 6.9 to 26 mg m^{-2}, while snow thickness averaged around 35 ± 5 cm. Based on the relationship between $K_d(PAR)$ and $\mathrm{TChl}a_{0-3\mathrm{cm}}$ in Ehn and Mundy (2013), we calculated a transmittance of $T = 0.65\%$ (6.9 mg m^{-2}) and $T = 0.41\%$ (26 mg m^{-2}) for the bottom ice algae layer (3 cm). Such an increase in ice algae biomass in the bottom sea ice layer would thus account for a decrease in transmittance by a factor of 1.6, half the decrease due to snowfall.

During the 2015 (2016) snow melt period, transmittance increased by a factor of 25 (20) from about 0.18% (0.3%) to more than 4.6% (6%). During the melt pond period, transmittance increased by a factor of 1.6 (4.3) up to 7.5% (26%). The lower 2015 values are due to sampling ending before the ice breakup. Melt ponds forming over sea ice increased the light transmittance in the water column, in agreement with Nicolaus et al. (2012) but at a slower rate compared to the snow melt period. Additionally, we showed that an increase in cloud cover can decrease both $PAR(0^+)$ and under-ice $PAR(1.3m)$ by a factor of two (Section 3.1).

In summary, our findings demonstrate that the snow thickness had the most significant attenuation contribution and largely controlled the spring under-ice light availability, in agreement with literature (i.e., Mundy et al., 2005; Leu et al., 2015; Hancke et al., 2018).

4.4. Bloom dynamics: from environmental conditions to algal biomass

Here we discuss the environmental conditions that likely controlled the algal bloom dynamics. The ice algal and phytoplankton phenology seemed similar for both years and can be divided into three main phases, but contrasting environmental conditions between 2015 and 2016 might explain the differences in the bloom magnitude and distribution. An illustration of the main environmental factors driving the evolution of the phytoplankton bloom is shown in **Figure 10**.

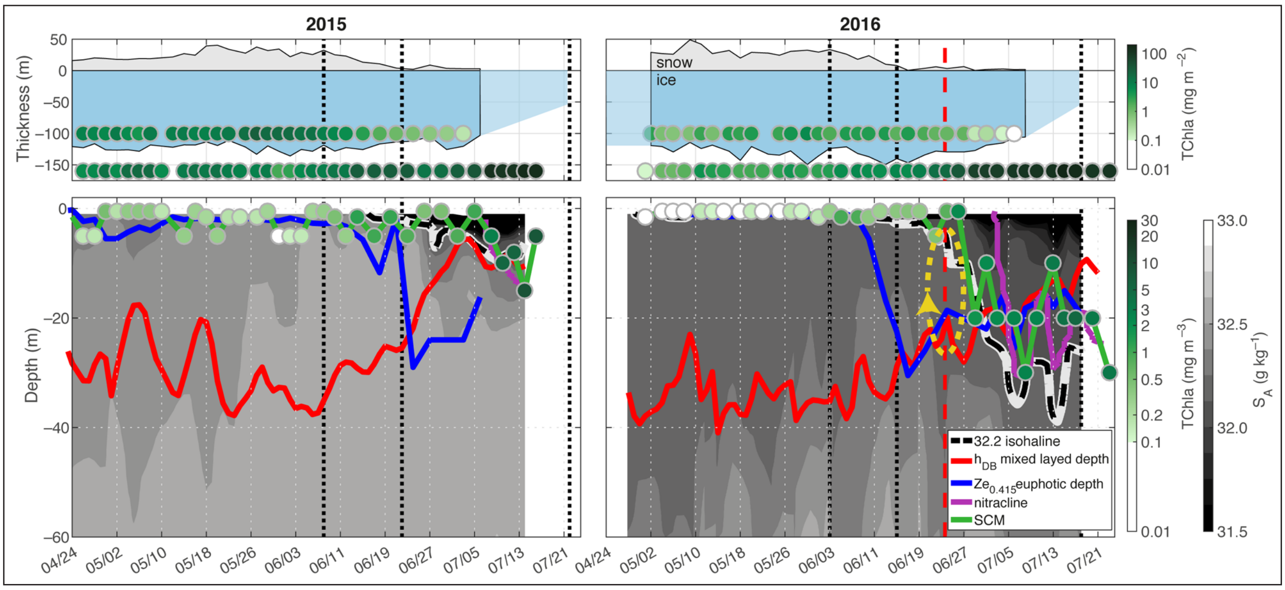

Figure 10: Representation of the algal bloom dynamics. The top panels illustrate for 2015 (left) and 2016 (right) the snow and sea ice evolution with vertically integrated ice algal (0–3 cm, blue background) and phytoplankton (surface to deepest measurement, white background) biomass in a green palette. Light blue areas correspond to periods with no data on sea ice. The bottom panels show the temporal evolution in the water column: the 32.2 isohaline, a proxy for freshwater, is a dashed black line; the equivalent mixed layer depth h_{BD} is in red; the euphotic depth $Z_{0.415}$ is represented by the isolume 0.415 mol photons m^{-2} d^{-1} in blue; the nitrate concentration of 1 µmol L^{-1} isoline (nitracline) is in magenta; the subsurface chlorophyll maximum (SCM) and corresponding [TChla_w] (mg m^{-3}) are in green. The mixing layer inferred from the SCAMP sampling during a 13-h period (vertical red dashed line) is represented by the yellow arrow. Vertical dotted lines chronologically represent snow melt initiation, melt pond initiation and sea ice breakup. Dates are month/day. DOI: https://doi.org/10.1525/elementa.372.f10

- **Snow-covered period.** Moderate TChl$a_{0–3cm}$ values around 4–10 mg m^{-2} were observed in April 2015, when winter conditions still prevailed. This finding agrees with recent results from Hancke et al. (2018) who observed ice algal accumulation in low-light conditions and thick snow cover (>15 cm). The ice algal bloom reached a maximum of 26 mg m^{-2} in 2015 and 6 mg m^{-2} in 2016 in late May. The average ice algal biomass was about four times higher in 2015, which was likely due to better light conditions (thinner snow cover until mid-May) in 2015 and, potentially, an early sloughing event prior to the commencement of observations in 2016. This result confirms the negative relationship between snow depth and ice algae biomass during its early development phase found by Campbell et al. (2015). In 2015, bulk ice nutrient concentrations correlated with ice algal biomass (TChl$a_{0–3cm}$; $r_{[NO_3^- + NO_2^-]} = 0.8$; $r_{[PO_4^{3-}]} = 0.74$, $r_{[Si(OH)_4]} = 0.47$; $p < 10^{-3}$) and showed elevated concentrations in the ice bottom relative to those in the interface water, suggesting that a nutrient 'concentration mechanism' was at play in sea ice. Similar observations have been made previously and have been suggested to be associated with a release of intracellular pools due to osmotic shock during ice melt processing (Cota et al., 1990, 2009; Harrison et al., 1990; Pineault et al., 2013; Torstensson et al., 2019) or via production of biofilms by sea ice diatoms and bacteria that potentially trap nutrients (Krembs et al., 2002, 2011; Steele et al., 2014). Bacterial activity may also have played a role through nutrient remineralization (Fripiat et al. 2014, 2017; Firth et al., 2016). By reducing the light transmitted to the upper water column, the snowfall in mid-May constrained phytoplankton growth to the very surface. For both years, the pre-bloom period was characterized by a much deeper h_{BD} (~30 m) than $Z_{0.415}$ that was located close to the surface. In those conditions, vertical mixing could potentially export phytoplankton out of the euphotic layer and disrupt phytoplankton growth (Behrenfeld and Boss, 2018). In general, we observed low biomass (≤0.5 mg m^{-3}) in both years, with a maximum at the surface.
- **Snow melt period.** This period was characterized by a rapid snow melt that led to the near-disappearance of the snow on the sea ice surface. The progression strongly increased the amount of light transmitted to the upper water column by more than one order of magnitude and significantly deepened $Z_{0.415}$ (**Figure 10**) demonstrating the major role of snow on light transmission (Mundy et al., 2005; Leu et al., 2015). For example, in 2016, the greater amount of winter precipitation, warmer air temperatures, and the earlier melt onset led to a more pronounced and earlier deepening of $Z_{0.415}$. In line with previous studies in Resolute Passage (Fortier et al., 2002; Galindo et al., 2014; Mundy et al., 2014), on Green Edge data (Galindo et al., 2017) or at pan-Arctic scale (Leu et al., 2015), the snow melt onset also coincided with the effective end of the ice algal bloom, possibly be-

cause of a brine flushing as indicated by the decrease in brine salinity resulting in an ablation of ice algal habitat. The ice algae then sloughed from the sea ice into the underlying water column. The concurrent increase in phytoplankton [TChla_w] in surface water at that specific time may have resulted from this release of ice algae. The possible seeding of the phytoplankton spring bloom by ice algae (e.g., Olsen et al., 2017; van Leeuwe et al., 2018; Selz et al., 2018) is beyond the scope of the present paper (but see Grondin, 2019). Freshwater from snow and ice melt started to accumulate at the ocean surface by the end of the period, and was subsequently warmed by solar radiation. About one week later, phytoplankton biomass started to accumulate in the upper water column, which was newly stratified as evidenced by the shoaling of h_{BD}.

- **Melt pond period.** Melt ponds started to form from snow meltwater around the summer solstice. Consequently, this period was characterized by a continuous increase in transmitted *PAR(1.3m)* (**Figure 2E**), and a deep $Z_{0.415}$ which reached a maximum of about 30 m in mid-June. Some cloudy periods, demonstrated by a local decrease in $PAR(0^+)$ during the second half of June 2016, may have temporarily dampened this shoaling of $Z_{0.415}$. After June, $Z_{0.415}$ shoaled to 20 m because of the phytoplankton accumulation that increased seawater light attenuation. The sea ice melting rate accelerated the freshening of the ocean surface layer. As meltwaters accumulated increasingly in the surface layer, stratification increased and the h_{BD} shoaled from 20–30 m to about 10–20 m at about the same depth as $Z_{0.415}$.

The surface layer stratified by meltwater seemed to provide sufficient stability on average for phytoplankton growth and blooming in the euphotic zone, which rapidly consumed most of the nutrients. Increasing stratification in the euphotic zone could also prevent the supply of nutrient-rich deeper water (Randelhoff et al., 2016). A subsurface chlorophyll maximum (SCM) formed at the base of the surface mixed layer, corresponding to the best compromise between light and nutrient availability (McLaughlin and Carmack, 2010; Martin et al., 2012). Over time, the SCM progressively deepened while nutrients were consumed down to 20–40 m, following the top of the nitracline and the euphotic depth pattern until the ice breakup (**Figure 10**). Both the SCM and nitracline deepened earlier to a greater depth in 2016 than in 2015, which may be attributed to a larger spring tide-induced vertical mixing (Mundy et al., 2014) and to an earlier phytoplankton bloom initiation (earlier $Z_{0.415}$ deepening and stratification). In this context, phytoplankton were able to reach a greater depth and a larger nutrient reservoir in 2016.

For both years, the concomitant increase in stratification (by two orders of magnitude) and irradiance (by three orders of magnitude) seemed to control the timing of phytoplankton bloom initiation (i.e., positive biomass accumulation rate, sensu Boss and Behrenfeld, 2010; Figure S17). The phytoplankton bloom seemed to be triggered earlier in 2016 (Figure S17). The differences between 2015 and 2016 must be considered carefully, as the sampling periods were different between years. In both years, the blooms peaked at about the same time and magnitude (152 mg TChla_w m^{-2} on 12 July 2015 and 182 mg TChla_w m^{-2} on 13 July 2016), and showed quasi-similar biomass when averaged over the same period (~30 and 38 mg TChla_w m^{-2}, respectively).

The significant phytoplankton blooms largely dominated the ice algal blooms in terms of maximum integrated biomass, reaching about 6–30 times the magnitude of the ice algal blooms. This work confirms previous estimations of the moderate contribution of sea ice algae in seasonally ice-covered water (e.g., Michel et al., 2006; Loose et al., 2011; Mundy et al., 2014) and contributes to the understanding of under-ice phytoplankton spring blooms as major and regular events under landfast sea ice in Baffin Bay (Wassmann and Reigstad, 2011; Leu et al., 2015; Horvat et al., 2017). Previous studies have documented similar magnitudes of ice algal blooms (~5–40 mg Chl*a* m^{-2}; Mundy et al., 2014; Leu et al., 2015) and phytoplankton blooms (~400–500 mg Chl*a* m^{-2}; Fortier et al., 2002; Mundy et al., 2014) in the Canadian Arctic Archipelago. Based on results of the companion article (Randelhoff et al., 2019), the ice-edge bloom located farther east in the marginal ice zone in 2016 reached ~70 mg TChla_w m^{-2}, less than half of the amount measured in this study (182 mg TChl*a* m^{-2}), therefore corroborating previous estimations that under-ice and ice-edge blooms can have comparable magnitudes (Mayot et al., 2018). Also possible is that the large amount of biomass accumulated at the study site may be attributed to low or mismatched secondary production.

5. Summary and Conclusions

During the Green Edge expeditions, we documented for the first time the temporal evolution of environmental factors driving the microalgal bloom in the sea ice-covered western Baffin Bay subject to rapid seasonal and interannual changes. Sampling a wide range of physical, chemical and biological parameters during the two contrasting years of 2015 and 2016 offered a unique opportunity to compare the succession of events that led to the under-ice algal spring blooms. The contrasting seasonal progression led to the different timing and magnitude of the blooms.

First of all, the atmospheric forcings during the preceding winters pre-conditioned the sea ice algal bloom differently for each year. The winter of 2014–2015 was colder with less snowfall than the 2015–2016 winter. As a consequence, twice the amount of light was transmitted to the bottom ice and the average ice algal biomass in 2015 was more than four times higher than in 2016. Our findings illustrate the critical need for year-round *in situ* sampling, especially to get a better understanding of the incorporation of sea ice algae into the sea ice during its formation and possible early brine drainage at the end of winter, and the impact of these physical processes on ice algal development.

Beneath the sea ice, the water at the study site displayed characteristics that, as expected, were representative of the hydrological conditions in offshore western Baffin Bay. The water column was largely influenced by the inflowing ArW modulated by spring-neap tidal currents. We observed differences between years: in 2016, the water column was more influenced by Pacific Waters and experienced more than 30% faster current velocities compared with 2015. The snow melt onset marked the termination of the ice algal bloom (likely sloughed in the water column) and a concomitant phytoplankton bloom initiation in the surface of the water column, typically linked to an increase in both stratification and light availability. Whereas more PAR penetrated the sea ice immediately after the onset of snow melt, biomass did not accumulate significantly until the onset of haline stratification and hence the reduction of mixing (i.e., melt pond period). This study underlines the major role of snow in vertical light attenuation compared to that of the sea ice, melt ponds, or even the ice algae themselves in the landfast sea ice of western Baffin Bay. Strong stratification due to meltwater accumulation was found to inhibit the supply of nutrients to the surface water layer, which became depleted in nutrients about two weeks after the snow melt onset. Spring tides enhanced the mixing of meltwaters with underlying ArW, resulting in a deeper surface layer reaching 40 m in 2016. The phytoplankton then developed at sub-surface following the best compromise between light and nutrient availability. Once the ice broke up at the end of the sampling period in July, the depth of the sub-surface chlorophyll maximum further deepened in the marginal ice zone, while meltwaters accumulated in the surface layer (see Randelhoff et al., 2019).

The significant phytoplankton blooms largely dominated the ice algal blooms in terms of maximum integrated biomass. This study also illustrates that under-ice phytoplankton blooms can reach similar or even greater magnitude than ice-edge blooms in marginal ice zones, contributing to the understanding of under-ice phytoplankton spring blooms as major and regular events under landfast sea ice in Baffin Bay. With the ongoing warming climate in the Arctic, the general trend toward thinner sea ice, longer open-water periods (Stroeve and Notz, 2018) and less snowfall (Bintanja, 2018) would drastically increase the availability of light and affect microalgal growth beneath the Baffin Bay sea ice cover. We can expect that an earlier onset of ice melt may shorten the sea ice algal growth season yet increase the potential for under-ice phytoplankton blooms in Baffin Bay.

Data Accessibility Statement

All data are accessible at the Green Edge database (http://www.obs-vlfr.fr/proof/php/GREENEDGE/greenedge.php) and will be made public after publication.

Supplemental files

The supplemental files for this article can be found as follows:

- **Figure S1.** 'True color' Landsat 8 Snapshots of the study site area in 2015. DOI: https://doi.org/10.1525/elementa.372.s1
- **Figure S2.** 'True color' Sentinel-2 Snapshots of the study site area in 2016. DOI: https://doi.org/10.1525/elementa.372.s1
- **Figure S3.** Time series of ANP "Arctic N-P relationship" based on nutrient sampling. DOI: https://doi.org/10.1525/elementa.372.s1
- **Figure S4.** Winter (late April) 'baseline' of the vertical hydrographic structure. DOI: https://doi.org/10.1525/elementa.372.s1
- **Figure S5.** Two-year time series of air temperature, wind speed, sea ice concentration, and daily total precipitation. DOI: https://doi.org/10.1525/elementa.372.s1
- **Figure S6.** Winter air temperature anomalies. DOI: https://doi.org/10.1525/elementa.372.s1
- **Figure S7.** SAR images from Sentinel-1 of the southwestern Baffin Bay area. DOI: https://doi.org/10.1525/elementa.372.s1
- **Figure S8.** Time series of transmittance, snow thickness and ice algal concentration. DOI: https://doi.org/10.1525/elementa.372.s1
- **Figure S9.** Hydrographic temporal evolution of the entire water column. DOI: https://doi.org/10.1525/elementa.372.s1
- **Figure S10.** Characterization of the dominant tidal waves. DOI: https://doi.org/10.1525/elementa.372.s1
- **Figure S11.** Depth evolution of tidal currents magnitude and direction. DOI: https://doi.org/10.1525/elementa.372.s1
- **Figure S12.** Temporal evolution of nutrients in seawater. DOI: https://doi.org/10.1525/elementa.372.s1
- **Figure S13.** Estimation of the depth integrated biomass bias from HPLC. DOI: https://doi.org/10.1525/elementa.372.s1
- **Figure S14.** Modelled synoptic circulation in Baffin Bay. DOI: https://doi.org/10.1525/elementa.372.s1
- **Figure S15.** Closest distance between the study site and the sea ice edge. DOI: https://doi.org/10.1525/elementa.372.s1
- **Figure S16.** Bulk salinity against in situ temperature across all sections of all ice cores. DOI: https://doi.org/10.1525/elementa.372.s1
- **Figure S17.** Phytoplankton accumulation rate. DOI: https://doi.org/10.1525/elementa.372.s1

Acknowledgements

This project would not have been possible without the support of the Hamlet of Qikiqtarjuaq and the members of the community as well as the Inuksuit School and its Principal Jacqueline Arsenault. The community contributed to the scientific campaign by facilitating logistical support and sharing local knowledge. The project is conducted under the scientific coordination of the Canada Excellence Research Chair in Remote Sensing of Canada's New

Arctic frontier and the CNRS and Université Laval Takuvik Joint International laboratory (UMI3376). We thank Françoise Pinczon du Sel and Eric Brossier from Vagabond for assistance in the field and Yves Christen for fixing our valuable snowmobiles. We also thank Guislain Bécu (Takuvik), Pascal Guillot (UQAR-ISMER), Shawn Mederic (Amundsen Science) for the data processing and quality control of the C-OPS, CTD and ADCP respectively. We thank Caroline Sévigny for deploying the SCAMP, José Luis Lagunas for deploying the ADCP, and Christian Haas for sharing the time-lapse pictures of the study site area. The field campaign was successful thanks to the contribution of F. Bruyant, J. Larivière, E. Rehm, C. Aubry, C. Lalande, A. LeBaron, C. Marty, J. Sansoulet, D. Christiansen-Stowe, A. Wells, M. Benoît-Gagné, and E. Devred from the Takuvik laboratory. We also thank Michel Gosselin, Québec-Océan, the CCGS *Amundsen* and the Polar Continental Shelf Program for their in-kind contribution in polar logistic and scientific equipment. We thank all participants in the Green Edge campaign for their contribution to the field work and data collection.

Funding information

The Green Edge project is funded by the following French and Canadian programs and agencies: ANR (Contract #111112), CNES (project #131425), IPEV (project #1164), CSA, Fondation Total, ArcticNet, LEFE and the French Arctic Initiative (Green Edge project). L. Oziel's postdoctoral fellowship is funded by an NSERC/CRSNG 'Visiting Fellowship' in a Canadian Laboratory (DFO) and supported by the joint Laboratory Takuvik, The Canada Excellence Research Chair in remote sensing of Canada's new Arctic Frontier. S.L. Girard was supported by a postdoctoral fellowship from NSERC/CRSNG. D. Dumont is funded by a NSERC Discovery Grant 402257-2013. This work was also supported by MEOPAR through its Observation Core.

Competing interests

The authors have no competing interests to declare.

Author contributions

L.O. and M.B. led the design of the study. Most of the data were formatted by P.M. L.O. led the writing, to which P.M and A.R. contributed. L.O. led the analysis and made the figures with contributions from P.M., A.R., L.L, and A.V. M-H.F. and J.F. led the sampling. J.F. provided continuous help for gathering the data. A.V. and D.D led sampling of the SCAMP data. Y.C., D.D. and P.B-A. helped in the interpretation of the ADCP and SCAMP data. P.M. and S.L-G. contributed to the light section such as the processing of the PAR, the transmittance, and the ice algal attenuation. All authors revised the earlier version of the manuscript, helped in the interpretation and approved the final version for publication.

References

Aminot, A and **Kérouel, R.** 2007. Dosage automatique des nutriments dans les eaux marines: méthodes en flux continu. Ed. Ifremer, *Méthodes d'analyse en milieu marin*, 188.

Arrigo, KR, Perovich, DK, Pickart, RS, Brown, ZW, van Dijken, GL, Lowry, KE, Mills, MM, Palmer, MA, Balch, WM, Bahr, F, Bates, NR, Benitez-Nelson, C, Bowler, B, Brownlee, E, Ehn, JK, Frey, KE, Garley, K, Laney, SR, Lubelczyk, L, Mathis, J, Matsuoka, A, Mitchell, BG, Moore, GWK, Ortega-Retuerta, E, Pal, S, Polashenski, CM, Reynolds, RA, Schieber, B, Sosik, HM, Stephens, M and **Swift, GH.** 2012. Massive phytoplankton blooms under Arctic sea ice. *Science* **336**(6087): 1408. DOI: https://doi.org/10.1126/science.1215065

Arrigo, KR, Perovich, DK, Pickart, RS, Brown, ZW, van Dijken, GL, Lowry, KE, Mills, MM, Palmer, MA, Balch, WM, Bates, NR, Benitez-Nelson, CR, Brownlee, E, Frey, KE, Laney, SR, Mathis, J, Matsuoka, A, Mitchell, BG, Moore, GWK, Reynolds, RA, Sosik, HM and **Swift, JH.** 2014. Phytoplankton Blooms beneath the Sea Ice in the Chukchi Sea. *Deep Sea Research Part II: Topical Studies in Oceanography* **105**: 1–16. ISSN 0967-0645. The Phytoplankton Megabloom beneath Arctic Sea Ice: Results from the ICESCAPE Program. DOI: https://doi.org/10.1016/j.dsr2.2014.03.018

Assmy, P, Fernández-Méndez, M, Duarte, P, Meyer, A, Randelhoff, A, Mundy, CJ, Olsen, LM, Kauko, HM, Bailey, A, Chierici, M, Cohen, L, Doulgeris, AP, Ehn, JK, Fransson, A, Gerland, S, Hop, H, Hudson, SR, Hughes, N, Itkin, P, Johnsen, G, King, JA, Koch, BP, Koenig, Z, Kwasniewski, S, Laney, SR, Nicolaus, M, Pavlov, AK, Polashenski, CM, Provost, C, Rösel, A, Sandbu, M, Spreen, G, Smedsrud, LH, Sundfjord, A, Taskjelle, T, Tatarek, A, Wiktor, J, Wagner, PM, Wold, A, Steen, H and **Granskog, MA.** 2017. Leads in Arctic Pack Ice Enable Early Phytoplankton Blooms below Snow-Covered Sea Ice. *Scientific Reports* **7**(40850). DOI: https://doi.org/10.1038/srep40850

Bates, SS and **Cota, FC.** 1986. Fluorescence induction and photosynthetic responses of Arctic ice algae to sample treatment and salinity. *J Phycol* **70**: 421–429. DOI: https://doi.org/10.1111/j.1529-8817.1986.tb02484.x

Behrenfeld, MJ and **Boss, ES.** 2018. Student's tutorial on bloom hypotheses in the context of phytoplankton annual cycles. *Glob Change Biol* **24**(1): 55–77. DOI: https://doi.org/10.1111/gcb.13858

Bélanger, S, Babin, M and **Tremblay, J-É.** 2013. Increasing cloudiness in Arctic damps the increase in phytoplankton primary production due to sea ice receding. *Biogeosciences* **10**(6): 4087–4101. DOI: https://doi.org/10.5194/bg-10-4087-2013

Bintanja, R, Katsman, CA and **Selten, FM.** 2018. Increased Arctic precipitation slows down sea ice melt and surface warming. *Oceanography* **31**(2): 118–125. DOI: https://doi.org/10.5670/oceanog.2018.204

Boss, E and **Behrenfeld, M.** 2010. In situ evaluation of the initiation of the North Atlantic phytoplankton bloom. *Geophys Res Lett* **37**(18): n/a–n/a. ISSN 00948276. 742. DOI: https://doi.org/10.1029/2010GL044174

Bouffard, D and **Boegman, L.** 2013. A diapycnal diffusivity model for stratified environmental flows. *Dynamics of Atmospheres and Oceans* **61–62**: 14–34. DOI: https://doi.org/10.1016/j.dynatmoce.2013.02.002

Brainerd, KE and **Michael, CG.** 1995. Surface mixed and mixing layer depths. *Deep Sea Res Pt I* **42**(9): 1521–1543. ISSN 0967-0637. DOI: https://doi.org/10.1016/0967-0637(95)00068-H

Campbell, KL, Mundy, CJ, Barber, DG and **Gosselin, M.** 2014. Remote estimates of ice algae biomass and their response to environmental conditions during spring melt. *Arctic* **67**(3): 375–387. DOI: https://doi.org/10.14430/arctic4409

Campbell, KL, Mundy, CJ, Barber, DG and **Gosselin, M.** 2015. Characterizing the sea ice algae chlorophyll *a*–snow depth relationship over Arctic spring melt using transmitted irradiance. *J Mar Syst* **147**: 76–84. DOI: https://doi.org/10.1016/j.jmarsys.2014.01.008

Carmack, E and **Wassmann, P.** 2006. Food webs and physical–biological coupling on pan-Arctic shelves: unifying concepts and comprehensive perspectives. *Prog Oceanogr* **71**: 446–477. DOI: https://doi.org/10.1016/j.pocean.2006.10.004

Collins, AK, Hannah, CG and **Greenberg, D.** 2011. Validation of a high-resolution modelling system for tides in the Canadian Arctic Archipelago. *Can Tech Rep Hydrogr Ocean Sci* **273**: vii + 72pp.

Cota, GF, Anning, JL, Harris, LR, Harrison, WG and **Smith, REH.** 2009. Impact of ice algae on inorganic nutrients in seawater and sea ice in Barrow Strait, NWT, Canada, during spring. *Can J Fish Aquat Sci* **47**(7): 1402–1415. DOI: https://doi.org/10.1139/f90-159

Cox, GFN and **Weeks, WF.** 1983. Equations for determining the gas and brine volumes in sea-ice samples. *J Glaciol* **29**(102): 306–316. DOI: https://doi.org/10.3189/S0022143000008364

Cullen, JJ and **Lewis, MR.** 1988. The kinetics of algal photoadaptation in the context of vertical mixing. *J Plankton Res* **10**: 1039–1063. DOI: https://doi.org/10.1093/plankt/10.5.1039

Curry, B, Lee, CM, Petrie, B, Moritz, RE and **Kwok, R.** 2014. Multiyear volume, liquid freshwater, and sea ice transports through Davis Strait, 2004–10. *J Phys Oceanogr* **44**(4): 1244–1266. DOI: https://doi.org/10.1175/JPO-D-13-0177.1

Cuypers, Y, Bouruet-Aubertot, P, Marec, C and **Fuda, JL.** 2012. Characterization of turbulence from a fine-scale parameterization and microstructure measurements in the Mediterranean Sea during the BOUM experiment. *Biogeosciences* **9**(8): 3131–3149. ISSN 1726-4189. DOI: https://doi.org/10.5194/bg-9-3131-2012

Dupont, F. 2012. Impact of sea-ice biology on overall primary production in a biophysical model of the pan-Arctic Ocean. *J Geophys Res* **117**: C00D17. DOI: https://doi.org/10.1029/2011JC006983

Ehn, JK and **Mundy, CJ.** 2013. Assessment of light absorption within highly scattering bottom sea ice from under-ice light measurements: implications for Arctic ice algae primary production. *Limnol Oceanogr* **58**: 893–902. DOI: https://doi.org/10.4319/lo.2013.58.3.0893

Ehn, JK, Mundy, CJ, Barber, DG, Hop, H, Rossnagel, A and **Stewart, J.** 2011. Impact of horizontal spreading on light propagation in melt pond covered seasonal sea ice in the Canadian Arctic. *J Geophys Res* **116**: C00G02. DOI: https://doi.org/10.1029/2010JC006908

Fernández-Méndez, M, Katlein, C, Rabe, B, Nicolaus, M, Peeken, I, Bakker, K, Flore, H and **Boetius, A.** 2015. Photosynthetic production in the Central Arctic during the record sea-ice minimum in 2012. *Biogeosciences* **12**: 2897–2945. DOI: https://doi.org/10.5194/bgd-12-2897-2015

Firth, E, Carpenter, SD, Sørensen, HL, Collins, RE and **Deming, JW.** 2016. Bacterial use of choline to tolerate salinity shifts in sea-ice brines. *Elem Sci Anth* **4**: 000120. DOI: https://doi.org/10.12952/journal.elementa.000120

Fortier, M, Fortier, L, Michel, C and **Legendre, L.** 2002. Climatic and biological forcing of the vertical flux of biogenic particles under seasonal Arctic sea ice. *Mar Ecol Progr Ser* **225**(1): 1–16. DOI: https://doi.org/10.3354/meps225001

Frey, KE, Perovich, DK and **Light, B.** 2011. The spatial distribution of solar radiation under a melting Arctic sea ice cover. *Geophys Res Lett* **38**(22): 1–6. DOI: https://doi.org/10.1029/2011GL049421

Fripiat, F, Meiners, KM, Vancoppenolle, M, Papadimitriou, S, Thomas, DN, Ackley, SF, Arrigo, KR, Carnat, G, Cozzi, S, Delille, B, Dieckmann, GS, Dunbar, RB, Fransson, A, Kattner, G, Kennedy, H, Lannuzel, D, Munro, DR, Nomura, D, Rintala, J-M, Schoemann, V, Stefels, J, Steiner, N and **Tison, J-L.** 2017. Macro-nutrient concentrations in Antarctic pack ice: Overall patterns and overlooked processes. *Elem Sci Anth* **5**: 13. DOI: https://doi.org/10.1525/elementa.217

Fripiat, F, Sigman, DM, Fawcett, SE, Rafter, PA, Weigand, MA and **Tison, JL.** 2014. New insights into sea ice nitrogen biogeochemical dynamics from the nitrogen isotopes. *Global Biogeochem Cy* **28**(2): 115–130. DOI: https://doi.org/10.1002/2013GB004729

Galindo, V, Gosselin, M, Lavaud, J, Mundy, CJ, Else, B, Ehn, J, Babin, B and **Rysgaard, S.** 2017. Pigment composition and photoprotection of Arctic sea ice algae during spring. *Mar Ecol Progr Ser* **585**: 49–69. DOI: https://doi.org/10.3354/meps12398

Galindo, V, Levasseur, M, Mundy, CJ, Gosselin, M, Tremblay, JÉ, Scarratt, M, Gratton, Y, Papakiriakou, T, Poulin, M and **Lizotte, M.** 2014. Biological and physical processes influencing sea ice, under-ice algae, and dimethyl-sulfoniopropionate during spring in the Canadian Arctic Archipelago. *J Geophys Res* **119**: 3746–3766. DOI: https://doi.org/10.1002/2013JC009497

Garrison, DL and **Buck, KR.** 1986. Organism losses during ice melting: a serious bias in sea ice community studies. *Polar Biol* **6**: 237–239. DOI: https://doi.org/10.1007/BF00443401

Gilbert, R. 1982. Contemporary sedimentary environments on Baffin Island, N.W.T., Canada: glaciomarine processes in fiords of eastern Cumberland Peninsula. *Arctic Alpine Res* **14**: 1–12. https://www.jstor.org/stable/1550809. DOI: https://doi.org/10.2307/1550809

Gourdal, M, Crabeck, O, Lizotte, M, Galindo, V, Babin, M, Scarratt, M, Gosselin, M, Scarratt, M and **Levasseur, M.** 2019. Upward transport of bottom ice dimethyl sulfide during the advanced melting stage of arctic first-year sea ice. *Elem Sci Anth* (in press). DOI: https://doi.org/10.1525/elementa.370

Grondin, PL. 2019. Algal taxonomic succession and its drivers during under-ice spring blooms in Baffin Bay. Msc thesis, Laval University.

Hancke, K, Lund-Hansen, LC, Lamare, ML, Højlund Pedersen, S, King, MD, Andersen, P and **Sorrell, BK.** 2018. Extreme low light requirement for algae growth underneath sea ice: A case study from Station Nord, NE Greenland. *J Geophys Res-Oceans* **123**: 985–1000. DOI: https://doi.org/10.1002/2017JC013263

Harrison, WG, Cota, GF and **Smith, REH.** 1990. Nitrogen utilization in ice algal communities of Barrow Strait, Northwest Territories, Canada. *Mar Ecol Progr Ser* **67**(3): 275–283. DOI: https://doi.org/10.3354/meps067275

Hooker, SB, Morrow, JH and **Matsuoka, A.** 2013. Apparent optical properties of the Canadian Beaufort Sea – Part 2: The 1% and 1 cm perspective in deriving and validating AOP data products. *Biogeosciences* **10**: 4511–4527. DOI: https://doi.org/10.5194/bg-10-4511-2013

Horvat, C, Jones, DR, Iams, S, Schroeder, D, Flocco, D and **Feltham, D.** 2017. The frequency and extent of sub-ice phytoplankton blooms in the Arctic Ocean. *Sci Adv* **3**: e1601191. DOI: https://doi.org/10.1126/sciadv.1601191

Jardon, FP, Vivier, F, Vancoppenolle, M, Lourenço, A, Bouruet-Aubertot, P and **Cuypers, Y.** 2013. Full-depth desalination of warm sea ice. *J Geophys Res-Oceans* **118**(1): 435–447. DOI: https://doi.org/10.1029/2012JC007962

Katlein, C, Arndt, S, Nicolaus, M, Perovich, DK, Jakuba, MV, Suman, S, Elliott, S, Whitcomb, LL, McFarland, CJ, Gerdes, R, Boetius, A and **German, CR.** 2015. Influence of Ice Thickness and Surface Properties on Light Transmission through Arctic Sea Ice. *Journal of Geophysical Research: Oceans* **120**(9): 5932–5944. ISSN 21699275. DOI: https://doi.org/10.1002/2015JC010914

Kirk, JTO. 2011. Light and Photosynthesis in Aquatic Ecosystems, 3rd edn. Cambridge: Cambridge University Press, 151. DOI: https://doi.org/10.1017/CBO9781139168212

Krembs, C, Eicken, H and **Deming, JW.** 2011. Exopolymer alteration of physical properties of sea ice and implications for ice habitability and biogeochemistry in a warmer Arctic. *Proc Natl Acad Sci USA* **108**(9): 3653–3658. DOI: https://doi.org/10.1073/pnas.1100701108

Krembs, C, Eicken, H, Junge, K and **Deming, JW.** 2002. High concentrations of exopolymeric substances in Arctic winter sea ice: implications for the polar ocean carbon cycle and cryoprotection of diatoms. *Deep-Sea Res Pt I* **49**(12): 2163–2181. ISSN 0967-0637. DOI: https://doi.org/10.1016/S0967-0637(02)00122-X

Kwok, R. 2018. Arctic sea ice thickness, volume, and multiyear ice coverage: losses and coupled variability (1958–2018). *Environ Res Lett* **13**: 105005. DOI: https://doi.org/10.1088/1748-9326/aae3ec

Lacour, L, Claustre, H, Prieur, L and **D'Ortenzio, F.** 2015. Phytoplankton biomass cycles in the North Atlantic subpolar gyre: a similar mechanism for two different blooms in the Labrador Sea. *Geophys Res Lett* **42**: 5403–5410. DOI: https://doi.org/10.1002/2015GL064540

Lacour, T, Lariviére, J and **Babin, M.** 2017. Growth, Chl *a* content, photosynthesis, and elemental composition in polar and temperate microalgae. *Limnol Oceanogr* **62**: 43–58. DOI: https://doi.org/10.1002/lno.10369

Laliberté, J, Bélanger, S and **Frouin, R.** 2016. Evaluation of satellite-based algorithms to estimate photosynthetically available radiation (PAR) reaching the ocean surface at high northern latitudes. *Remote Sens Environ* **184**: 199–211. DOI: https://doi.org/10.1016/j.rse.2016.06.014

Landy, JC, Ehn, JK and **Barber, DG.** 2015. Albedo feedback enhanced by smoother Arctic sea ice. *Geophys Res Lett* **42**(24): 10,714–10,720. DOI: https://doi.org/10.1002/2015GL066712

Leppäranta, M and **Manninen, T.** 1988. The brine and gas content of sea ice with attention to low salinities and high temperatures. Internal Rep 88-2, Helsinki: Finn Inst Mar Res.

Letelier, RM, Karl, DM, Abbott, MR and **Bidigare, RR.** 2004. Light driven seasonal patterns of chlorophyll and nitrate in the lower euphotic zone of the North Pacific Subtropical Gyre. *Limnol Oceanogr* **49**(2): 508–519. ISSN 00243590. DOI: https://doi.org/10.4319/lo.2004.49.2.0508

Leu, E, Mundy, C, Assmy, P, Campbell, K, Gabrielsen, T, Gosselin, M, Juul-Pedersen, T and **Gradinger, R.** 2015. Arctic spring awakening: Steering principles behind the phenology of vernal ice algal blooms. *Progr Oceanog* **139**: 151–170. ISSN 0079-6611. DOI: https://doi.org/10.1016/j.pocean.2015.07.012

Loose, B, Miller, LA, Elliott, S and **Papakyriakou, T.** 2011. Sea ice biogeochemistry and material transport across the frozen interface. *Oceanography* **24**(3): 202–218. DOI: https://doi.org/10.5670/oceanog.2011.72

Martin, J, Tremblay, J-É and **Price, NM.** 2012. Nutritive and photosynthetic ecology of subsurface chlorophyll maxima in Canadian Arctic waters.

Biogeosciences **9**: 5353–5371. DOI: https://doi.org/10.5194/bg-9-5353-2012

Massicotte, P, Bécu, G, Lambert-Girard, S, Leymarie, E and **Babin, M.** 2018. Estimating underwater light regime under spatially heterogeneous sea ice in the Arctic. *Appl Sci* **8**(12): 2693. DOI: https://doi.org/10.3390/app8122693

Matrai, P and **Apollonio, S.** 2013. New estimates of microalgae production based upon nitrate reductions under sea ice in Canadian shelf seas and the Canada Basin of the Arctic Ocean. *Mar Biol* **160**(6): 1297–1309. DOI: https://doi.org/10.1007/s00227-013-2181-0

Matthes, LC, Ehn, JK, Girard, SL, Pogorzelec, NM, Babin, M and **Mundy, CJ.** 2019. Average cosine coefficient and spectral distribution of the light field under sea ice: Implications for primary production. *Elem Sci Anth* 7: 25. DOI: https://doi.org/10.1525/elementa.363

Mayot, N, Matrai, P, Ellingsen, IH, Steele, M, Johnson, K, Riser, SC and **Swift, D.** 2018. Assessing phytoplankton activities in the seasonal ice zone of the Greenland Sea over an annual cycle. *J Geophys Res-Oceans* **123**: 8004–8025. DOI: https://doi.org/10.1029/2018JC014271

McLaughlin, FA and **Carmack, EC.** 2010. Deepening of the nutricline and chlorophyll maximum in the Canada Basin interior, 2003–2009. *Geophys Res Lett* **37**: L24602. DOI: https://doi.org/10.1029/2010GL045459

Meier, WN. 2016. Losing Arctic sea ice: Observations of the recent decline and the long-term context. In: Thomas, DN (ed.), *Sea Ice*, 3rd Edition. John Wiley & Sons Ltd, 290–303. DOI: https://doi.org/10.1002/9781118778371.ch11

Michel, C, Ingram, RG and **Harris, LR.** 2006. Variability in oceanographic and ecological processes in the Canadian Arctic Archipelago. *Progr Oceanogr* **71**(2–4): 379–401. DOI: https://doi.org/10.1016/j.pocean.2006.09.006

Miller, LA, Fripiat, F, Else, B, Bowman, JS, Brown, KA, Collins, RE, Ewert, M, Fransson, A, Gosselin, M, Lannuzel, D, Meiners, KM, Michel, C, Nishioka, J, Nomura, D, Papadimitriou, S, Russell, LM, Sørensen, LL, Thomas, DN, Tison, J-L, van Leeuwe, MA, Vancoppenolle, M, Wolff, EW and **Zhou, J.** 2015. Methods for biogeochemical studies of sea ice: The state of the art, caveats, and recommendations. *Elem Sci Anth* **3**: 000038. DOI: https://doi.org/10.12952/journal.elementa.000038

Morel, A and **Smith, RC.** 1974. Relation between total quanta and total energy for aquatic photosynthesis. *Limnol Oceanogr* **19**: 591–600. DOI: https://doi.org/10.4319/lo.1974.19.4.0591

Morozov, EG and **Paka, VT.** 2010. Internal waves in a high-latitude region. *Oceanology* **50**(5): 668–674. Available at: http://link.springer.com/10.1134/S0001437010050048. DOI: https://doi.org/10.1134/S0001437010050048

Münchow, A, Falkner, KK and **Melling, H.** 2015. Baffin Island and West Greenland Current Systems in northern Baffin Bay. *Progr Oceanogr* **132**: 305–317. ISSN 0079-6611. DOI: https://doi.org/10.1016/j.pocean.2014.04.001

Mundy, CJ, Barber, DG and **Michel, C.** 2005. Variability of snow and ice thermal, physical and optical properties pertinent to sea ice algae biomass during spring. *J Mar Syst* **58**: 107–120. DOI: https://doi.org/10.1016/j.jmarsys.2005.07.003

Mundy, CJ, Ehn, JK, Barber, DG and **Michel, C.** 2007. Influence of snow cover and algae on the spectral dependence of transmitted irradiance through Arctic landfast first-year sea ice. *J Geophys Res* **112**: C03007. DOI: https://doi.org/10.1029/2006JC003683

Mundy, CJ, Gosselin, M, Ehn, J, Gratton, Y, Rossnagel, A, Barber, DG, Martin, J, Tremblay, J-É, Palmer, M, Arrigo, KR, Darnis, G, Fortier, L, Else, B and **Papakyriakou, T.** 2009. Contribution of under-ice primary production to an ice-edge upwelling phytoplankton bloom in the Canadian Beaufort Sea. *Geophys Res Lett* **36**(17). ISSN 0094-8276. DOI: https://doi.org/10.1029/2009GL038837

Mundy, CJ, Gosselin, M, Gratton, Y, Brown, K, Galindo, V, Campbell, K, Levasseur, M, Barber, D, Papakyriakou, T and **Bélanger, S.** 2014. Role of environmental factors on phytoplankton bloom initiation under landfast sea ice in Resolute Passage, Canada. *Mar Ecol Prog Ser* **497**: 39–49. DOI: https://doi.org/10.3354/meps10587

Newton, R, Schlosser, P, Mortlock, R, Swift, J and **MacDonald, R.** 2013. Canadian Basin freshwater sources and changes: Results from the 2005 Arctic Ocean Section. *J Geophys Res-Oceans* **118**(4): 2133–2154. DOI: https://doi.org/10.1002/jgrc.20101

Nicolaus, M, Katlein, C, Maslanik, J and **Hendricks, S.** 2012. Changes in Arctic sea ice result in increasing light transmittance and absorption. *Geophys Res Lett* **39**: L24501. DOI: https://doi.org/10.1029/2012GL053738

Olsen, LM, Laney, SR, Duarte, P, Kauko, HM, Fernández-Méndez, M, Mundy, CJ, Rösel, A, Meyer, A, Itkin, P, Cohen, L, Peeken, I, Tatarek, A, Różańska-Pluta, M, Wiktor, J, Taskjelle, T, Pavlov, AK, Hudson, ST, Granskog, MA, Hop, H and **Assmy, P.** 2017. The role of multiyear ice in the seeding of icealgae blooms in Arctic pack ice. *J Geophys Res-Biogeo* **122**(7): 1529–1548. DOI: https://doi.org/10.1002/2016JG003668

Osborn, TR. 1980. Estimates of the local rate of vertical diffusion from dissipation measurements. *J Phys Oceanogr* **10**(1): 83–89. ISSN 0022-3670. DOI: https://doi.org/10.1175/1520-0485(1980)010<0083:EOTLRO>2.0.CO;2

Pawlowicz, R, Beardsley, B and **Lentz, S.** 2002. Classical tidal harmonic analysis including error estimates in MATLAB using T_TIDE. *Comput Geosci* **28**: 929–937. DOI: https://doi.org/10.1016/S0098-3004(02)00013-4

Peralta-Ferriz, C and **Woodgate, RA.** 2015. Seasonal and interannual variability of pan-Arctic surface mixed layer properties from 1979 to 2012 from hydrographic data, and the dominance of stratification for multiyear mixed layer depth shoaling. *Prog Oceanogr* **134**: 19–53. DOI: https://doi.org/10.1016/j.pocean.2014.12.005

Petrich, C and **Eicken, H.** 2010. Growth, Structure and Properties of Sea Ice. In: Thomas, DN and Dieckmann, GS (eds.), *Sea Ice – An Introduction to its Physics, Chemistry, Biology and Geology*, Second Edition. Oxford: Blackwell Science Ltd, 23–77. DOI: https://doi.org/10.1002/9781444317145.ch2

Petrich, C and **Eicken, H.** 2017. Overview of sea ice growth and properties. In: Thomas, DN (ed.), *Sea Ice*, 3rd Edition. John Wiley & Sons Ltd, 1–41. DOI: https://doi.org/10.1002/9781118778371.ch1

Pineault, S, Tremblay, JE, Gosselin, M, Thomas, H and **Shadwick, E.** 2013. The isotopic signature of particulate organic C and N in bottom ice: Key influencing factors and applications for tracing the fate of ice-algae in the Arctic Ocean. *J Geophys Res-Oceans* **118**: 287–300. DOI: https://doi.org/10.1029/2012JC008331

Post, E, Bhatt, US, Bitz, CM, Brodie, JF, Fulton, TL, Hebblewhite, M, Kerby, J, Kutz, SJ, Stirling, I and **Walker, DA.** 2013. Ecological consequences of sea-ice decline. *Science* **341**: 519–525. DOI: https://doi.org/10.1126/science.1235225

Randelhoff, A, Fer, I and **Sundfjord, A.** 2017. Turbulent upper-ocean mixing affected by meltwater layers during Arctic summer. *J Phys Oceanogr* **47**(4): 835–853. DOI: https://doi.org/10.1175/JPO-D-16-0200.1

Randelhoff, A, Fer, I, Sundfjord, A, Tremblay, JÉ, Reigstad, M. 2016. Vertical fluxes of nitrate in the seasonal nitracline of the Atlantic sector of the Arctic Ocean. *J Geophys Res-Oceans* **121**(7): 5282–5295. ISSN 2169-9291. DOI: https://doi.org/10.1002/2016JC011779

Randelhoff, A, Oziel, L, Massicotte, P, Bécu, G, Galí, M, Lacour, L, Dumont, D, Vladoiu, A, Marec, C, Bruyant, F, Houssais, M-N, Tremblay, J-É, Deslongchamps, G and **Babin, M.** 2019. The evolution of light and vertical mixing across a phytoplankton ice-edge bloom. *Elem Sci Anth*, **7**(1): 20. DOI: https://doi.org/10.1525/elementa.357

Ras, J, Uitz, J and **Claustre, H.** 2008. Spatial variability of phytoplankton pigment distributions in the Subtropical South Pacific Ocean: comparison between in situ and modelled data. *Biogeosciences* **5**: 353–369. DOI: https://doi.org/10.5194/bg-5-353-2008

Ricchiazzi, P, Yang, SR, Gautier, C and **Sowle, D.** 1998. SBDART: a research and teaching software tool for plane-parallel radiative transfer in the Earth atmosphere. *B Am Meteorol Soc* **79**: 2101–2114. DOI: https://doi.org/10.1175/1520-0477(1998)079<2101:SARATS>2.0.CO;2

Riebesell, U. 1989. Comparison of sinking and sedimentation rate measurements in a diatom winter/spring bloom. *Mar Ecol Prog Ser* **54**: 109–119. DOI: https://doi.org/10.3354/meps054109

Ruddick, B, Anis, A and **Thompson, K.** 2000. Maximum Likelihood Spectral Fitting: The Bachelor Spectrum. *J Atmos Ocean Tech* **17**: 1541–1555. DOI: https://doi.org/10.1175/1520-0426(2000)017<1541:MLSFTB>2.0.CO;2

Selz, V, Saenz, BT, van Dijken, GL and **Arrigo, KR.** 2018. Drivers of ice algal bloom variability between 1980 and 2015 in the Chukchi Sea. *J Geophys Res-Oceans* **123**(10): 7037–7052. DOI: https://doi.org/10.1029/2018JC014123

Serreze, MC and **Meier, WN.** 2019. The Arctic's sea ice cover: trends, variability, predictability, and comparisons to the Antarctic. *Ann NY Acad Sci* **1436**(1): 36–53. DOI: https://doi.org/10.1111/nyas.13856

Søreide, JE, Leu, E, Berge, J, Graeve, M and **Falk-Petersen, S.** 2010. Timing of blooms, algal food quality and *Calanus glacialis* reproduction and growth in a changing Arctic. *Glob Change Biol* **16**(11): 3154–3163. DOI: https://doi.org/10.1111/j.1365-2486.2010.02175.x

Spreen, G, Kaleschke, L and **Heygster, G.** 2008. Sea ice remote sensing using AMSR-E 89-GHz channels. *J Geophys Res* **113**(C2): C02S03. DOI: https://doi.org/10.1029/2005JC003384

Steele, DJ, Franklin, DJ and **Underwood, GJC.** 2014. Protection of cells from salinity stress by extracellular polymeric substances in diatom biofilms. *Biofouling* **30**(8): 987–998. DOI: https://doi.org/10.1080/08927014.2014.960859

Stroeve, J and **Notz, D.** 2018. Changing state of Arctic sea ice across all seasons. *Environ Res Lett* **13**(10): 103001. DOI: https://doi.org/10.1088/1748-9326/aade56

Tang, CL, Ross, CK, Yao, T, Petrie, B, DeTracy, BM and **Dunlap, E.** 2004. The circulation, water masses and sea-ice of Baffin Bay. *Progr Oceanogr* **63**(4): 183–228. DOI: https://doi.org/10.1016/j.pocean.2004.09.005

Torstensson, A, Young, JN, Carlson, LT, Ingalls, AE and **Deming, JW.** 2019. Use of exogenous glycine betaine and its precursor choline as osmoprotectants in Antarctic sea-ice diatoms. *J Phycol* **55**(3): 663–675. DOI: https://doi.org/10.1111/jpy.12839

Tremblay, J-É, Anderson, LG, Matrai, P, Coupel, P, Bélanger, S, Michel, C and **Reigstad, M.** 2015. Global and regional drivers of nutrient supply, primary production and CO_2 drawdown in the changing Arctic Ocean. *Progr Oceanogr* **139**: 171–196. ISSN 0079-6611. DOI: https://doi.org/10.1016/j.pocean.2015.08.009

van Leeuwe, MA, Tedesco, L, Arrigo, KR, Assmy, P, Campbell, Meiners, KM, Rintala, JM, Selz, V, Thomas, DN and **Stefels, J.** 2018. Microalgal community structure and primary production in Arctic and Antarctic sea ice: A synthesis. *Elem Sci Anth* **6**: 4. DOI: https://doi.org/10.1525/elementa.267

Verin, G, Dominé, F, Picard, G, Arnaud, L and **Babin, M.** 2019. Metamorphism of Arctic marine snow during the melt season: Impact on albedo. *The Cryosphere (in review)*. DOI: https://doi.org/10.5194/tc-2019-113

Wassmann, P and **Reigstad, M.** 2011. Future Arctic Ocean seasonal ice zones and implications for pelagic-benthic coupling. *Oceanography* **24**: 220–231. DOI: https://doi.org/10.5670/oceanog.2011.74

Wu, Y, Tang, C and **Hannah, C.** 2012. The circulation of eastern Canadian seas. *Progr Oceanogr* **106**: 28–48. DOI: https://doi.org/10.1016/j.pocean.2012.06.005

How to cite this article: Oziel, L, Massicotte, P, Randelhoff, A, Ferland, J, Vladoiu, A, Lacour, L, Galindo, V, Lambert-Girard, S, Dumont, D, Cuypers, Y, Bouruet-Aubertot, P, Mundy, C-J, Ehn, J, Bécu, G, Marec, C, Forget, M-H, Garcia, N, Coupel, P, Raimbault, P, Houssais, M-N and Babin, M. 2019. Environmental factors influencing the seasonal dynamics of spring algal blooms in and beneath sea ice in western Baffin Bay. *Elem Sci Anth,* 7: 34. DOI: https://doi.org/10.1525/elementa.372

Domain Editor-in-Chief: Jody W. Deming, School of Oceanography, University of Washington, US

Knowledge Domain: Ocean Science

Part of an *Elementa* Special Feature: Green Edge

Submitted: 23 April 2019 **Accepted:** 09 August 2019 **Published:** 27 August 2019

ELEMENTA
Science of the Anthropocene

Elem Sci Anth is a peer-reviewed open access journal published by University of California Press.

OPEN ACCESS